UCLouvain

epl

École polytechnique de Louvain

Impact of hydrogen blending on the cyclic variability of an EGR diluted methanol SI engine

An experimental study

Authors: **Bastien Morineau, Maxime Spira**
Supervisors: **Francesco Contino, Hervé Jeanmart**
Readers: **Mauro Daese, Maxime Pochet, Sara Spano**
Academic year 2021–2022
Master [120] in Mechanical Engineering

Abstract

In the climate crisis context, reducing Green House Gas emissions is of paramount importance. "Green Deal" was signed in Europe, imposing a 100% reduction in GHGs by 2035. This is the equivalent of a ban on all internal combustion engines. This decision will be re-evaluated in 2026, and electrofuels could be part of the balance. One of the most promising is methanol.

Compared to other electrofuels such as hydrogen, methanol remains liquid at Standard Temperature and Pressure, making its storage practical.

The present work addresses the use of methanol in Spark Ignition engines. Its use in parallel with Exhaust Gas Recirculation for Nitrous Oxides reduction is studied. With large fractions of EGR, combustion stability deteriorates. The introduction of hydrogen blending as a means to stabilize combustion is then also investigated. A test bench is modified, and a complete fuel line is implemented for this purpose.

The experimental results showed that the IMEP and IE decrease slightly with EGR with pure methanol while they increase with the hydrogen/methanol mixture. An increase in IE from 33 to 37.3% is noticed for the largest EGR condition. The addition of hydrogen shortens the flame development and propagation times under EGR. Increasing the EGR fraction decreases the maximum in-cylinder temperature in both cases, demonstrating that EGR can effectively control NOx emissions in a hydrogen/methanol mixture. The cyclic variability with EGR was drastically reduced with the introduction of hydrogen, for a decrease from 7.8 to 3.6% in the highest diluted case.

Acknowledgments

First of all, we would like to sincerely thank Sara and Mauro who helped us through this master thesis. Sara's support and guidance throughout the year was valuable and helped us stay on course. We wish to thank Mauro for giving us the opportunity to work on his engine late in the year and for postponing his own experiments. Without his help, we would never have been able to do experimental work. His availability during these last months was inestimable.

Then we would like to express our gratitude to our thesis supervisors Prof. Hervé Jeanmart and Prof. Francesco Contino. Their feedback in meetings during the year was always relevant and helped us challenge ourselves. Their availability during trying times at the laboratory was priceless.

We also would like to thank Maxime Pochet for kindly accepting the role of reader and becoming part of the jury. A special thanks to the CREDEM technical staff, especially Frank, Julien, Arnaud, Hervé and Luc. Their help and advice for the implementation of the bench and fuel system were precious.

Finally, we would like to thank our respective friends, families and roommates for their support during the making of this thesis and our whole university path.

Contents

List of Figures

List of Tables

Nomenclature

Abbreviations

AFR Air Fuel Ratio

ATEX ATmosphère EXplosive

BCE Balanced Chemical Equation

BDC Bottom Dead Center

BMEP Break Mean Effective Pressure

BSFC Brake Specific Fuel Consumption

BTE Brake Thermal Efficiency

CAD Crank Angle Degree

CAE Crank Angle Encoder

CHR Cumulative Heat Release

CI Compression Ignition

COVimep Coefficient Of Variation in indicated mean effective pressure

CR Compression Ratio

DFT Direct Fourier Transform

DI Direct Injection

ECU Engine Control Unit

EGR Exhaust Gas Recirculation

EVC Exhaust Valve Closing

EVO Exhaust Valve Opening

FAR Fuel-to-Air Ratio

FAR_{st} Stoichiometric Fuel-to-Air Ratio

FFV Flex-Fuel vehicles

FIR Finite Impulse Response

FuelMEP Fuel Mean Effective Pressure

GHG Greenhouse Gas

HRR Heat Release Rate

ICE Internal Combustion Engine

IMEP Indicated Mean Effective Pressure

$IMEP_{gross}$ Gross Indicated Mean Effective Pressure

$IMEP_{net}$ Net Indicated Mean Effective Pressure

IVC Intake Valve Closing

IVO Intake Valve Opening

LC Least Count

LHV Lower Heating Value

MBF Mass Burned Fraction

MBT Maximum Brake Torque

MFC Mass Flow Controller

MPRR Maximum Pressure Rise Rate

P2F Power-to-Fuel

PFI Port Fuel Injection

ppm parts per million

PRR Pressure Rise Rate

RGF Residual Gas Fraction

RI Ringing Intensity

RoHR Rate of Heat Release

RON Research Octane Number

RPM Rotations Per Minute

SI Spark Ignition

SOC Start Of Combustion

SP Spark Plug

STP Standard Temperature and Pressure

TDC Top Dead Center

TWC Three Way Catalytic converter

VCR Variable Compression Ratio

WDI Water Direct Injection

WOT Wide Open Throttle

Greek letters

α Volume fraction

δ Ignition delay

γ Ratio of specific heat capacities

λ Air excess ratio

ϕ Equivalence Ratio

θ Crank angle position

Symbols

M_m Molar Mass

V_c Clearance volume

V_d Displacement volume

B Bore

n Number of moles

S Stroke

x Molar fraction

Introduction

The technological advances associated with over a century of industrialization have had significant environmental consequences. The growing use of fossil fuels, deforestation, and intensive agricultural activities have led to overall growth in GreenHouse Gas emissions (GHG), increasing Earth's average temperature. Human-induced warming reached approximately 1°C above pre-industrial levels in 2017 and will increase at an approximate 0.2°C per decade [1], while the amount of CO_2 in the atmosphere has risen from 280 ppm in 1850 to approximately 400 ppm today [2].

Reducing GHG emissions in all sectors is a necessary step toward stabilizing the average global surface temperature. As a result, the Paris Agreement established in 2015 a new legal framework with a very ambitious environmental objective [3]. It sets a global goal of limiting global warming well below 2°C above pre-industrial levels and encourages limiting the temperature increase to 1.5°C.
In line with these guidelines, the EU committed with its European Green Deal in 2019 to reduce net GHG in the EU by at least 55% by 2030 compared to 1990 levels and to become climate neutral by 2050 [4]. Reaching this target requires a transformation of European society and economy.

All sectors must strive to reduce fossil energy consumption and CO_2 emissions. In the transport industry, which is responsible for approximately 25% of GHG emissions [5], such emissions will have to be reduced by 100% in new cars sold in 2035 compared to their 2021 level. With the current state of technology, this reduction amounts to a ban on internal combustion engines from that date onwards, allowing only 100% electric or hydrogen fuel-cell powered cars. This decision will be reviewed in 2026, considering technological developments, thereby reconsidering the possible use of electrofuels.

Methanol, among other electrofuels, is being investigated for extensive use in Internal Combustion Engines (ICE). With the reduction of conventional ICE vehicles and the immediate need to achieve the strategic goal of carbon neutrality, the application of fuel methanol in ICE will inevitably grow. Therefore, research on methanol-fueled engines is of great significance and provides vast market opportunities in the coming years.

This master thesis presents the implementation of a methanol-fueled Spark Ignition (SI) engine and the study of the impact of hydrogen blend on combustion stability when the advanced combustion technique of synthetic Exhaust Gas Recirculation (EGR) is used.

Chapter 1 is a literature review and gives a background to this master thesis. The various ways of increasing engine efficiency are discussed, and the importance of alternative fuels in the transport sector, especially methanol.

Chapter 2 discusses the implementation of the SI engine and its associated modifications, the implementation of the methanol tank and supply system to the engine, along with the safety aspect of introducing a new fuel line. The general use of the test bench, with the different software used to run the engine, is also detailed. Finally, the experimental procedure is presented.

Chapter 3 explains how the raw engine pressure data is processed into the experimental results. The different required calibrations of the newly implemented engine are presented, as well as the several methodologies used to compute the important combustion parameters for the SI engine.

Chapter 4 presents the experimental results, starting with the pure methanol ignition sweep to find the Maximum Braque Torque (MBT) used for the subsequent experiments. The addition of synthetic EGR and hydrogen blend is then analyzed with a specific look at the cyclic variability. Finally, an uncertainty analysis is conducted over the injected mass as well as the Indicated Mean Effective Pressure (IMEP) and indicated efficiency.

Chapter 1

Literature review

In order to properly address this matter, the background is important to understand the motivation behind this project.

The world's energy supply faces several challenges. An excessive amount of energy comes from fossil fuels, concentrated in a few countries, leading to a high import dependency and a large amount of GHG transport emissions, contributing to climate change. While a decrease in GHG emissions was observed during the Covid-19 crisis, the emissions of the fourth quarter of 2021 already rose above the pre-Covid trends [6]. More CO_2 is emitted than can be recycled. In the transport sector, GHG emissions can be reduced by improving the efficiency of vehicles. The efficiency of today's vehicles can only be significantly improved by expensive technology which requires changes in power trains, such as electric cars with batteries or fuel cells, for example, hydrogen. Efficiency can also be increased to a lower extent with alternative fuels, which properties differ from conventional fuels, and well-known advanced combustion technologies. In the context given, methanol is a promising green fuel proposed to be studied in the context of carbon neutrality in an SI engine. However, the in-cylinder temperatures reached during combustion lead to the formation of NOx, a pollutant that is hazardous to health. It can be, therefore, necessary to reduce the temperature reached in the cylinder, which can be done through EGR. However, EGR induces a strong instability in the combustion. In order to decrease this instability, the introduction of hydrogen in the mixture can be beneficial.

The research question addressed in this master thesis is, therefore: 'How does the introduction of hydrogen into an EGR diluted methanol SI engine affect the combustion cyclic variability?'

The following sections discuss why solutions to increase engine efficiency significantly are more challenging to implement and why methanol as an electrofuel can be a solution towards carbon neutrality in the transport sector. Its properties, along with its use in ICEs, are addressed. Finally, EGR and hydrogen enrichment are discussed.

1.1 Methanol as an alternative fuel

As mentioned at the beginning of this chapter, there are ways to increase the efficiency of vehicles significantly and greatly reduce GHG emissions. These technologies, however, come with serious disadvantages.

Batteries have a very low energy density compared to liquid fuels, as shown in figure 1.1.

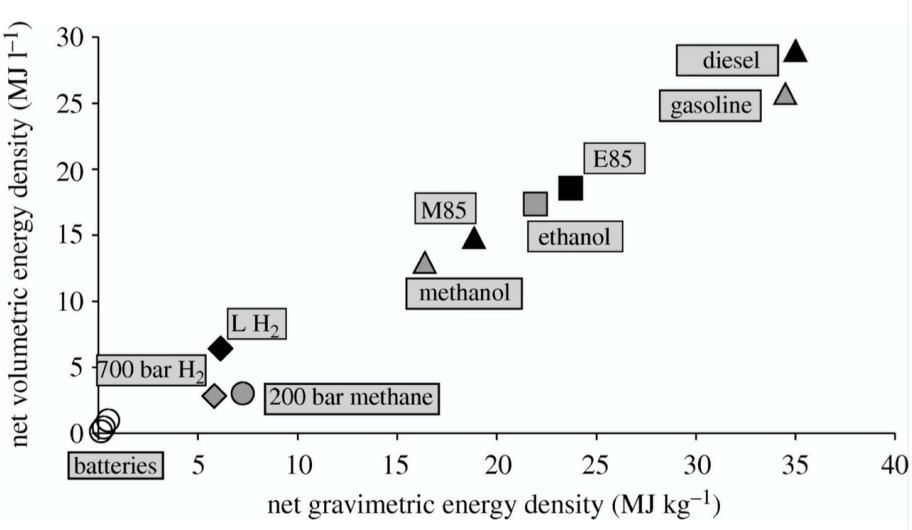

Figure 1.1: Several different energy sources are shown on this graph. It can be seen that batteries energy density is limited with respect to conventional fuels such as gasoline or diesel. From [7].

This would make it difficult for heavy trucks to use batteries for long-distance transportation. Added to this is their high cost. Indeed, the most optimistic estimation suggests a price between 100 and 135 €/kWh [8]. To reach a range similar to that of a conventional gasoline car with a 50 liters gasoline tank, a 100 kWh battery would be required and would cost more than 10000 €. Moreover, the primary raw materials used for batteries are available in limited supply on the planet, so it is somewhat unrealistic to assume that electrically powered ones can replace all conventional vehicles. Finally, there is no particularly suitable treatment method for used batteries. If they are not appropriately treated, they will eventually pollute the environment and the soil.

Compared to batteries, hydrogen has a higher energy density. However, it is still lower than other liquid fuels, even when liquefied. This is because hydrogen is much more difficult to store than, for example, gasoline. It can be stored as a gas at high pressure or as a liquid at extremely low temperatures in a cryogenic tank. Such storage systems add much weight to the device they are added to. It also requires much additional energy to pressurize the hydrogen or liquefy it. Liquid fuels at STP are the most cost-effective energy carriers.

Growth in the transport sector is expected in developing countries. By economic neces-

sity, vehicles in such countries must be based on low-cost powertrains and cheap fuel systems. Combustion engines are made from cost-effective materials and fuel systems and are hence ideal for this purpose.

Methanol as a fuel can provide an alternative to the challenges faced by the transport and energy sectors. A transition to methanol is possible through evolution rather than revolution. Current engines could run on methanol with a few modifications. It can also be perfectly mixed with gasoline; several flex-fuel vehicles have already been developed [9]. Methanol can improve engine power output and efficiency over gasoline fuel.

Unlike hydrogen, it is liquid under atmospheric conditions, making it compatible with current fuel systems. Another significant advantage is that it can be synthesized from biomass or via CO_2 capture, see Section 1.1.2. This provides great potential for CO_2 reduction and security of energy supply, as methanol can be produced worldwide.

The main challenge in becoming completely independent from fossil fuels is producing enough renewable energy, such as solar, wind, hydraulic, or geothermal energy. All of these energies are produced as electric power, and the major drawback of electric power is that it is very poorly stored. Methanol offers a solution as an energy vector in the same way that hydrogen is. In addition, methanol has the great advantage of being liquid and, therefore, easier to store and transport. Methanol has also become a research focus due to its high market demand, wide broad applicability, and potential for synthesizing important follow-up products. Methanol has powerful features regarding the economy, safety, environmental protection, reliability, and applicability. It is an ideal substitute for conventional internal combustion engines [10]. Olah et al. [11] therefore suggested a 'Methanol Economy' in which methanol has the role of:

- Energy storage material
- Fuel
- Hydrocarbons and their derived products

1.1.1 Methanol properties

The motivation for using methanol as a fuel comes from its attractive chemical, physical, and air-mixture properties. Its main properties, alongside gasoline, the most widely used fuels in SI engines, and hydrogen, can be found in the following Table 1.1.

Property	Units	Methanol	Gasoline	Hydrogen
Chemical formula		CH_3OH	Various	H_2
Molecular weight	$[kg/kmol]$	32.04	107	2.02
Density STP	$[kg/m^3]$	790	740	0.08
Vapour density STP	$[kg/m^3]$	1.42	3.88	0.08
Heat of vaporization	$[kJ/kg]$	1100	180-350	4.61
Oxygen content by mass	[%]	49.93	0	0
Lower Heating Value LHV	$[MJ/kg]$	20.09	42.9	120
Volumetric energy content	$[MJ/l]$	15.9	31.7	0.0096
Stoichiometric Air-Fuel Ratio	$[kg/kg]$	6.5	14.6	34.2
Auto-ignition temperature	[K]	738	466-743	858
Adiabatic flame temperature	[K]	2143	2175	2390
Energy per unit mass of air	$[MJ/kg]$	3.09	2.94	3.51
Heat of vaporization per unit mass of air	[kJ/kg]	169.2	12.3-24	13.48
Research Octane Number RON	[-]	111	95	130
Stoichiometric laminar flame speed	$[cm/s]$	42	28	nf

Table 1.1: Physical, chemical, air-fuel mixture and related to engine use properties for selected fuels. Adapted from Verhelst [9].

It can be seen that the volumetric energy density of methanol is almost half the one of gasoline. Also, methanol's Air-Fuel Ratio (AFR) is relatively low compared to gasoline. The mass of methanol per mass of air needed for complete combustion is 2.25 times higher than the one of gasoline. As the theoretical AFR of methanol is lower than that of gasoline, the theoretical AFR of mixed gas has a Lower Heating Value (LHV) equivalent to gasoline, allowing similar engine power to be maintained. This means the power can be kept when switching from gasoline to methanol without affecting performance/cruising range. The drawback is solely the reduced energy density of methanol which requires a larger tank capacity to allow the same performance/cruising range (approximately twice as large).

The high Research Octane Number (RON) of methanol, which indicates a higher resistance to knock and a longer auto-ignition delay, allows a methanol-fueled engine to operate at a higher Compression Ratio (CR) than a gasoline engine. A higher CR results in higher effective efficiency and higher power output.

Methanol contains a hydroxyl group, which makes it conductive and polar. Due to its high polarity, hydrogen bonds are formed, which makes methanol more stable than other hydrocarbons. This results in high latent heat of vaporization and low vapor pressure.

Methanol engines can therefore have cold start issued. The high latent heat of vaporization means that the intake air is better cooled, which positively affects the volumetric efficiency since cooling increases the density. However, the high polarity also results in high corrosivity against metals, which makes materials used in fuel systems an important consideration.

The laminar flame speed of methanol results in more isochoric combustion than gasoline, which increases the effective efficiency. The relatively wide ignition limits, in combination with the high flame speed, allow methanol engines to run at high dilutions with air (poor mixtures) or with EGR. Also, when burning methanol -and light alcohols in general- the combustion products have a higher ratio of triatomic molecules to diatomic molecules. As a result, the combustion products have a high heat capacity, which favorably influences the positive effect of EGR.

1.1.2 Sustainable methanol production

Methanol can be produced in a renewable way by hydrogenation of CO_2 and green H_2, with the following chemical reaction.

$$H_2O + CO_2 \longrightarrow CH_3OH \tag{1.1}$$

Using CO_2 to produce methanol reduces the GHG emissions and provides a wide range of clean chemicals and fuels [12]. The exhaust gases from fossil fuel power plants are used to obtain the CO_2 via capture technologies necessary for producing methanol. CO_2 could also be extracted from the atmosphere to synthesize methanol, but as the atmosphere contains only 0.038% of CO_2, it is industrially unfeasible/unrealistic.

Energy input is also required to produce H_2 by electrolysis and capture and release CO_2. Electrolysis can be performed with excess renewable energy, thus addressing the intermittent nature of renewable energies and helping stabilize the grid.

Emissions from transport, source to a power plant, the production process, transport to the consumer, and vehicle emissions of methanol production from fossil fuel and green energy have been assessed by Galindo Cifre et al. [13]. Fossil fuel-derived methanol has the highest emissions (3.8 kg CO_2/kg methanol), while methanol produced by capturing CO_2 has the lowest emissions (0.1 kg CO_2/kg methanol). Its atmospheric capture virtually cancels out CO_2 emissions from separation, liquefaction, and transport. Therefore, methanol can be seen as a product of the atmosphere. The following figure 1.2 depicts green methanol production and shows how beneficial it can be in the context of carbon neutrality.

It can be seen that CO_2 is captured from exhaust gases, hydrogen is produced from renewables, and green methanol is synthesized from both captured CO_2 and hydrogen. The methanol is burned in the engine and passed through the exhaust gas treatment device to generate CO_2. This CO_2 is captured and hydrogenated to produce methanol. Therefore, the combustion of methanol in internal combustion engines provides, in the ideal case, a

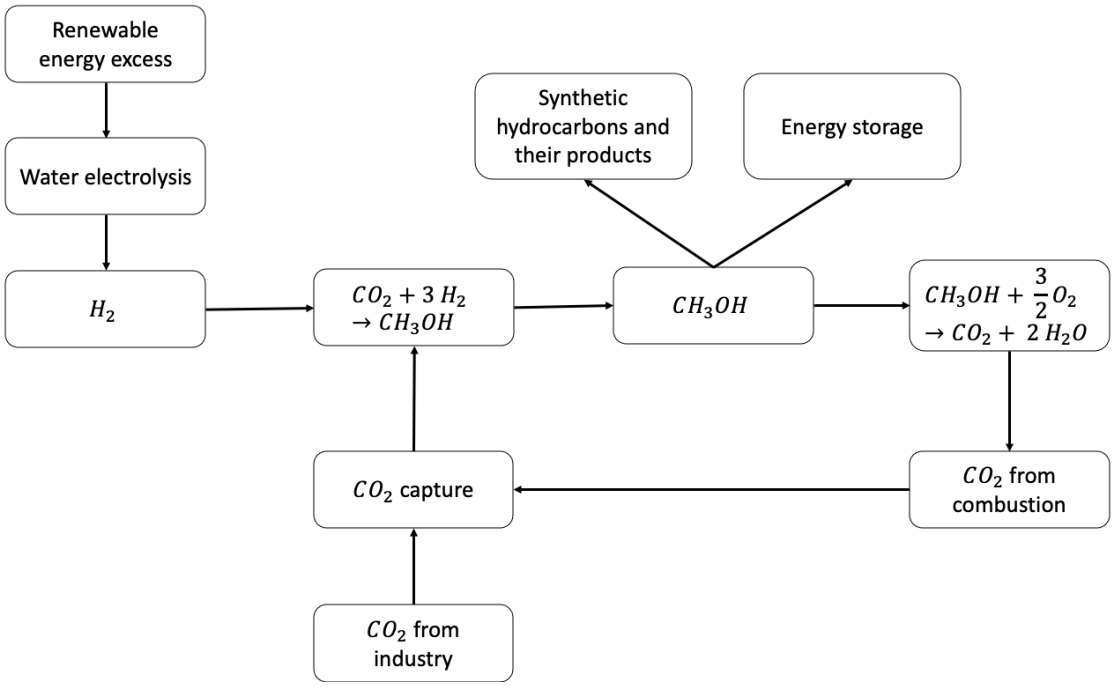

Figure 1.2: The process of hydrogenation of CO_2 to methanol with green hydrogen, including the carbon neutralization cycle of methanol.

carbon-neutral cycle without increasing CO_2 emissions [14]. Moreover, methanol is not only a good alternative fuel; it can act as energy storage and also be transformed into high-value-added chemicals, such as olefins and aromatics.

1.2 Methanol as a fuel for SI engines

Now that context is provided, the focus can shift to using methanol in SI engines. First, performance and characteristic emissions are discussed. Then, the disadvantages of methanol in its use in SI engines are presented. Finally, various ways of increasing methanol-fueled SI engine efficiencies are discussed

1.2.1 Pure methanol SI engines

Since methanol and gasoline have different properties, SI engines react differently to both fuels. Power, efficiency, and exhaust gas composition depend on it. Therefore, it is crucial to understand how methanol is used as fuel in SI engines.

The use of methanol in internal combustion engines varies, not only in terms of the fuel mixture but also in terms of engine design. A distinction is made between two types of engines: Flex-Fuel Vehicles (FFV) engines and dedicated pure methanol (M100) engines.

FFV engines are designed to run on both methanol and gasoline. They are slightly changed from conventional gasoline engines to run on methanol. In the process, the advantages of methanol are partially sacrificed. This is because properties such as a higher RON are not being fully exploited. Since these engines are also designed for gasoline with a significantly lower knock resistance than methanol, they have a lower CR. M100 engines do not consider gasoline limiting properties and hence allow higher CR, which results in better efficiency and fuel economy performance [15] as shown in Figure 1.3. With pure methanol, Brake Thermal Efficiency (BTE) of 43% is reached for a BMEP of 12 bar.

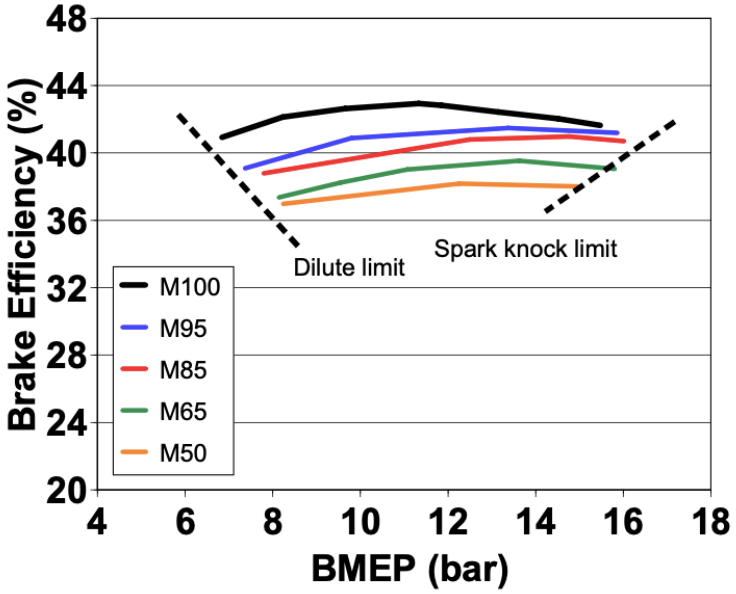

Figure 1.3: Brake thermal efficiency as a function of engine load for various methanol-gasoline blends, at 2000 rpm. From [15].

A compromise to work optimally with methanol and gasoline is using a Variable Compression Ratio (VCR). This is a technique whereby the CR is changed according to the fuel composition. However, the technological implementation of this technique is not straightforward, and the best results are obviously obtained in dedicated engines and will therefore be the consideration hereafter.

The first generation of M85 engines also showed considerable progress in power and efficiency, mainly due to the higher resistance of methanol to knocking. This resistance enabled them to achieve Maximum Brake Torque (MBT) timing over a wide range of operating points and allowed the CR to be increased to 12:1 and above. For instance, the Ford Escort M85 in 1981 produced 20% more power while being 15% more efficient than its gasoline equivalent [16].

Nakata et al. used E100 in a high CR naturally aspirated, Port Fuel Injection (PFI) SI engine [17]. They were able to use MBT timing and found that engine torque increased

by 20% compared to operation with 92 RON gasoline. The BTE at full load at 2,800 rpm was 39.6% and 31.7% with E100 and gasoline respectively. Even at operating points that were not limited by knocking, efficiency improvements of more than 3% were possible due to the advantages of faster flame speed and lower heat losses with ethanol.

Besides the advantages of knock resistance, the high burning rate and wider flammability limits of light alcohols open up alternative options for charge control, particularly for methanol [18]. Pannone et al. reported the results of an experimental lean-burn methanol turbocharged engine [19]. The reported BTE was up to 14% better than those of stoichiometrically fuelled engines with throttle load control. The exhaust Nitrous Oxide (NOx) penalty of the lean burn strategy was as high as 150%, which makes the operational use of such a strategy doubtful without advanced after-treatment like a lean NOx trap.

Still, Brusstar et al. demonstrated that it is more attractive to exploit the wider dilution limits of alcohols in a strategy using a stoichiometric fuel and EGR to control the charge, reducing throttling losses and allowing the use of a three-way catalyst for after-treatment. Using a 1.9-liter turbocharged diesel engine with a CR of 19.5:1 that was converted for SI operation with methanol [20]. The higher CR resulted in higher peak BTEs than the baseline diesel engine (40%) for methanol operation (42%). Similar peak BTEs were previously obtained by Koenig et al. on a dedicated methanol engine with a CR of 12:1 [21]. High levels of cooled EGR (up to 50%) were used to reduce knocking and pre-ignition issues and extend the high-efficiency regions to the part-load operating points. WOT operation was possible up to a BMEP of 6 bar. Similar work by Brusstar et al. on a converted 4.5-liter V6 diesel engine established WOT operation up to 4 bar BMEP with pure methanol [22].

Finally, formaldehyde (CH_2O) is produced during incomplete combustion of methanol which can lead to poisoning [23]. Also, aldehydes play a considerable role in the formation of photochemical smog. Compared with gasoline vehicles, pure methanol vehicles have significantly reduced CO, PM, and polycyclic aromatic hydrocarbon (PAH) emissions. Nevertheless, HC and NOx emissions are in the same range.

1.2.2 Drawbacks of methanol

Cold start issues

Methanol condensation in the intake valve and the cylinder is a concern when starting an engine at low ambient temperature as it can prevent the evaporation of methanol and lead to a non-combustible mixture at the ignition point. On the one hand, because of the low energy density of methanol, injecting more fuel to deliver the same power as in gasoline operation is necessary. On the other hand, because of the high latent heat of vaporization, it takes more energy to vaporize a given quantity of fuel. Both properties ensure that methanol requires much more energy to vaporize the fuel than gasoline. Combined with the low vapor pressure of methanol, this results in starting issues at low ambient temperatures.

Vapor pressure is the pressure that a substance's vapor exerts on the walls of a closed space. For fuels, this measures the ability to form a flammable mixture. The vapor pressure of methanol is shown in Figure 1.4.

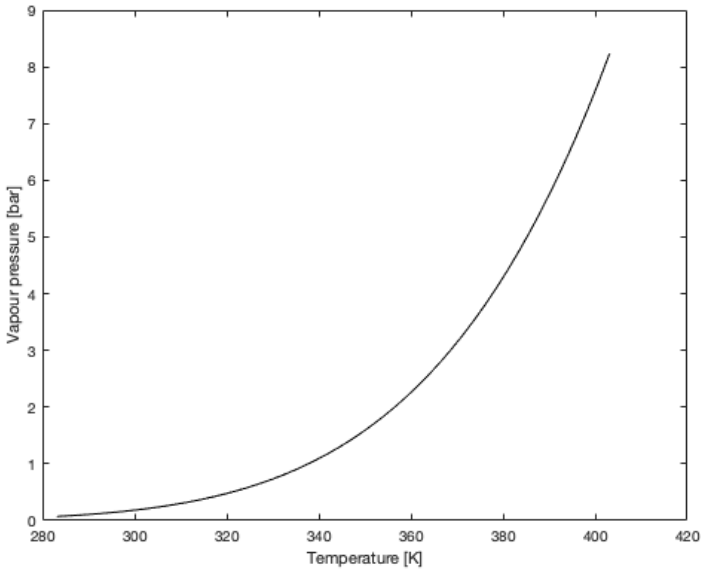

Figure 1.4: Vapour pressure computed with Antoine Equation.

Gasoline, unlike methanol, is a complex blend of light and heavy hydrocarbons. The light fractions such as heptane or butane in this mixture have higher vapor pressure (for a given temperature) than methanol. It allows evaporating at lower temperatures enhancing the formation of a flammable mixture in the cylinder.

In addition to its low vapor pressure, methanol is only flammable in air at volume percentages between 6.7 and 36 vol%, compared to gasoline, with a lower ignition limit of 1.3 vol%. As a result, a larger quantity of vaporized fuel is required to form a flammable mixture, further increasing the requirements for forming a flammable mixture at the ignition time. To enhance the evaporation process, the injection pressure can be increased. Those are generally comprised between 3 and 6 bar.

At ambient temperatures below 16°C, the methanol engine might not be successfully run without start-up aid because of insufficient formation of fuel-air mixtures [16].

In the case of the experiments conducted in this master thesis, the ambient temperature is between 25 to 35°C. Therefore, the cold start issue will not be addressed.

Material compatibility

Gasoline, unlike methanol, is a complex blend of light and heavy hydrocarbons. The light fractions such as heptane or butane in this mixture have higher vapor pressure (for a given temperature) than methanol. It allows evaporating at lower temperatures enhancing the formation of a flammable mixture in the cylinder.
-In methanol and alcohols, in general, the presence of a hydroxyl group causes polarity. Such polarity gives rise to properties such as a high boiling point and heat of vaporization, but also higher corrosiveness towards some materials than gasoline [24].

Therefore, it is necessary to consider which materials are resistant to methanol. Both metals and polymers can be damaged by using alcohol as fuel. This may fail some components in the engine. Even when parts do not fail, the corrosiveness of the material can cause the fuel to become contaminated. The deposits can cause wear and ultimately damage other components, particularly the fuel pump, and lubricity additives are needed to prevent its breakdown.

In general, ferrous metals show a higher corrosion rate when exposed to alcohol than gasoline. The polarity of methanol is a cause of (dry) corrosion, but often the corrosion is caused by ionic impurities such as chloride ions and acetic acid in the (aqueous) alcohols. A concentration of chloride ions, acetic acid, and ethyl acetate can produce a synergistic effect in aqueous methanol, causing corrosion much more significantly than with a single impurity. The formation of acetic acid and formic acid in the fuel can further increase its aggressive character [9]. Therefore, when running an engine with pure methanol or methanol blends, it is recommended to use methanol in its purest form.

As the methanol volumetric energy content is half of the gasoline, the injection duration of methanol fuel should be nearly double the gasoline for the same amount of power delivery; thus, a suitable injector design is required. For a similar driving condition as the gasoline vehicle, the larger fuel tank is required for methanol [25], as stated previously.

Spark plug choice

Early fresh mixture ignition takes place during the compression stroke before spark ignition. It is caused by heat from hot spots in the cylinder chamber, such as valves, spark plug electrodes, or deposits in the cylinder. Due to the lower ignition energy of methanol compared to gasoline, the likelihood of early ignition is higher in the presence of a hot spot. The spark plug electrode is generally the hottest point in the combustion chamber, with typical temperatures around 800 °C. Since the minimum ignition energy of methanol is almost half that of gasoline, such temperatures can cause premature ignition of methanol. The conventional solution to lower this temperature is a "cold type" spark plug with a higher heating range, as seen in Figure 1.5. The smaller insulator legs result in higher heat dissipation.

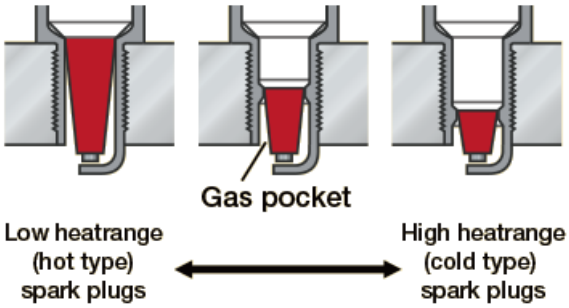

Figure 1.5: Heating range of spark plugs and its associated geometry.

1.3 Exhaust Gas Recirculation

EGR is a well-known technique used in ICEs. The following review introduces the concept and its application.

1.3.1 Pumping losses in SI engines

SI engines work under stoichiometric conditions. Usually, the fuel is supplied through PFI in the intake manifold, even if it becomes increasingly common to see Direct Injection (DI) in SI engines. As the Equivalence Ratio, defined as the actual Fuel-Air Ratio (FAR) divided by the stoichiometric FAR, must be maintained at a value of $\phi = 1$ at all times, the only way to control the load of the engine is by reducing the amount of air-fuel mixture entering the cylinder. A throttle valve is placed in the intake manifold inducing a pressure drop and limiting the flow rate [26]. As it opens, more air-fuel mixture (or air when DI is used) can pass through to the cylinders, and of course, the more it closes, the less mixture arrives in the combustion chamber.

Due to the inherent way of functioning of the SI engine, consequent losses are encountered when air passes through the throttle. This is particularly challenging at medium and low regimes as the throttle blocks the most air, and the most significant quantity of friction is encountered.

EGR is, therefore, a solution of interest. The objective is to decrease pumping losses by bringing combusted gases (mostly inert gases) to the intake so that the flow passing through the throttling system stays high at the part load range. This allows being with WOT as wide as possible as often as possible, i.e., for the largest range of conditions. Engines used in general transportation being rarely used at full-load, EGR can help increase efficiency and consequently save up to 4.6% of fuel consumption according to Climent et al. [27].

1.3.2 NOx management

Although EGR has useful applications in SI engines, it was initially conceived to reduce NOx formation in Compression Ignition (CI) engines. Since CI engines operate at low equivalence ratios, using a Three-Way Catalyst (TWC) to manage unburned hydrocarbons, carbon monoxide, and NOx emissions is not an option [28]. With the implementation of EGR, the inert gases added to the intake mixture decrease the peak temperature in the cylinder and the proportion of O_2 in the combustion chamber, thus reducing the amount of thermal NOx produced. Wei et al. [29]emphasize the importance of reducing the peak cylinder temperature, as for every 100 degrees K increase, the NO formation rate almost doubles.
Al-Qurashi et al. [30] highlight the three main effects of inert gas dilution through EGR:

- Thermal effect: increase in heat capacity of the oxidizer and reduction of flame temperature
- Dilution effect: reduction of the oxygen concentration
- Chemical effect: CO_2 being an active species, it participates in the combustion process

1.3.3 Knock control

Knocking is an abnormal combustion phenomenon taking place in SI engines. In spark ignition engines, combustion is initiated by the spark plug at the appropriate time. However, auto-ignition conditions may be encountered in parts of the mixture that have not yet been reached by the flame front, usually due to a hot spot caused by temperature or concentration non-uniformities. This self-ignition produces a sudden increase in pressure inside the cylinder inducing pressure waves and heat transfer. These phenomena lead to thermal stress and subsequent erosion, causing irreversible damage if not appropriately managed.

SI knocking differs from diesel knocking, resulting from a long ignition delay that allows fuel to accumulate in more considerable quantities in the combustion chamber and produces a higher Heat Release Rate (HRR) when ignition occurs. All references to knocking in this master thesis are to gasoline knocking.

Previously, knock could be limited by using an excess amount of fuel to decrease combustion In the past, knocking could be limited by using an excessive amount of fuel to lower the combustion temperature [29]. However, this method leads to higher fuel consumption and increased HC and CO emissions. Moreover, this technique is unnecessary since TWC is interesting in the stoichiometric ratio. With the increasing importance of pollution and environmental issues, such a solution must be rejected. EGR can help dilute the charge, lower the temperature inside the cylinder and reduce knocking while maintaining stoichiometric combustion.

1.3.4 EGR limit and cyclic variability

As EGR increases, flame speed is lowered, leading to risks of a misfire, a decrease in total efficiency, and high increases in HC emissions. Above a certain EGR rate, combustion becomes unstable and induces variability between cycles. This instability can be assessed with several parameters by measuring the cyclic variability's intensity. These parameters are classified into four main categories: pressure-related parameters, combustion-related parameters, flame front-related parameters, and exhaust-related parameters.

The cyclic variability of the IMEP is the most used parameter to indicate the engine behaviour on combustion in general and is defined [31] as

$$COV_{IMEP} = \frac{\sigma_{IMEP}}{\overline{IMEP}} \cdot 100\% = \frac{\sigma_{IMEP}}{\mu_{IMEP}} \tag{1.2}$$

It is common to find in the literature the limit of $\text{COV}_{IMEP} = 10\%$ as the limit of what is acceptable for use in ICE. Typical results of the COV_{IMEP} with respect to the EGR fraction are shown in Figure 1.6. If the COV_{IMEP} values increase too significantly, long-term damage to the engine can be expected. Jooris and Suijs [26] found that a methanol-fueled DISI engine would achieve a lower treshold of COV_{IMEP} of 5% for a volume fraction of about 30% EGR.

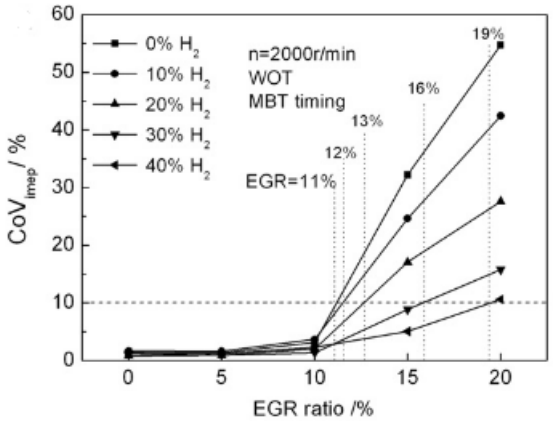

Figure 1.6: COV_{IMEP} as a function of EGR percentage for a SI engine fueled with natural gas-hydrogen blends. From [32].

1.3.5 Synthetic EGR

The gas that contributes most to the impact of EGR is CO_2, as explained by Al-Qurashi et al. [30]. Therefore, an interesting way to study EGR's effect on combustion processes and emissions is to replace it with COV_{IMEP} CO_2 dilution.
There are differences between CO_2 dilution and EGR that must be noted and considered. The temperature differences are considerable because EGR gases exit the cylinders, whereas CO_2 comes directly from a cylinder at room temperature. Exhaust gases from conventional SI engines are also composed of CO_2, but they contain nitrogen, carbon monoxide, and water vapor. Gong et al. [33] estimated that it takes about twice the

amount of CO_2 to achieve the same effect as EGR dilution on stoichiometric combustion parameters. They concluded that CO_2 dilution is more effective than EGR in reducing CO and HC emissions, although the opposite effect is observed for NOx emissions.

An effective way of approximating the real EGR while still being straightforward to implement is to add nitrogen to the CO_2 gas mixture supplied to the inlet. The only species in large quantities in the exhaust gas that does not appear in the intake with a synthetic CO_2-N_2 EGR is H_2O. This is the only species in the exhaust gas that is in a liquid state at room temperature. It is, therefore, deliberately decided not to add water vapor to the dilution process because of the complexity of implementing it on a test bench. Low concentration products such as CO, NOx, and SO_2, which are only found on a ppm scale, are also not considered in the synthetic EGR [34]. The remaining component in large quantities in the products is H_2O. The synthetic EGR being conducted thanks to CO_2 and N_2, the water vapor fraction is added to the CO_2 fraction to keep the fraction of nitrogen unchanged as it is the one that doesn't depend on combustion.

The synthetic EGR does not depend on the engine operating conditions since it comes from the intake manifold. As Zheng et al. [35] pointed out, simulated EGR cuts the intrinsic relationship between in-cylinder combustion quality and EGR composition. This allows for a smaller fluctuation of intake parameters throughout a set of cycles; therefore, the effects of dilution can be better analyzed.

1.4 Hydrogen enrichment

As mentioned earlier, unstable combustion, misfiring, and large cycle-to-cycle variability occur when EGR levels are too high. A way to overcome these issues is to add a small percentage of hydrogen to the mixture. Hydrogen has several properties that make it convenient to mix with methanol [36]. It has a wide flammability limit, which allows the methanol to burn lean, thus improving thermal efficiency and reducing emissions. Its fast combustion rate and high LHV allow improved combustion, overall thermal efficiency, brake mean effective pressure (BMEP), and reduced cycle-to-cycle variability (i.e., COVimep) [37, 14, 38].

Wang et al. [37] investigated the effect of CO_2 dilution on a hydrogen-enriched gasoline engine's combustion and emission characteristics. They found that a 3vol% hydrogen enrichment in a CO_2 diluted gasoline engine shortens the combustion time and strongly reduces the COVimep for the different CO_2 dilution levels tested. In addition, according to a numerical study by Tian et al. [36], hydrogen enrichment can reduce fuel consumption. They found that a blended methanol-H_2 SI engine could theoretically benefit from a 31.5% decrease in specific braking fuel consumption (BFSC) at 1500 RPM. It was also found that HC, CO, and CO_2 emissions would be reduced by hydrogen enrichment. However, NOx emissions increase steadily with increasing amounts of H_2 enrichment. This is contrary to the benefits that CO_2 dilution brings to combustion, so a balance must be found.

Park et al. [38] examined the effect of adding CO_2 to the combustion of a hydrogen-enriched natural gas engine for EGR simulation. The results revealed that NOx emissions decrease steadily when the CO_2 level increases. An appropriate increase in the proportion of CO_2 could help to increase the thermal efficiency of the hydrogen-enriched natural gas engine at slightly leaner mixtures. However, after adding CO_2, the thermal efficiency decreased at lean conditions. In these studies, increasing the proportion of CO_2 and inert gases in the cylinder was found to be effective in reducing NOx emissions from hydrogen-enriched natural gas engines.

Chapter 2

Experimental setup

In order to conduct the experiments, the SI engine bench running on methanol must be implemented, and the experiment intake parameters must be determined.
In the first part of this chapter, the modifications to the engine and the test bench are presented.
In the second part of the chapter, the experimental procedure and the determination of the input parameters to carry out the experiments.

2.1 Engine modification

The engine used is a Yanmar L100V diesel engine that has been modified to be converted to an SI engine. The main specifications of the Yanmar L100V are given in the table 2.1. When Badhuri [34] worked on the combustion of biomass syngas in an HCCI engine, he selected this engine for several reasons. Its industrial design supports an increased CR, for the simplicity of this single cylinder engine which allows simpler instrumentation and modifications for various jobs, and its price.
The same engine was chosen for subsequent internal combustion engine research so that the test bench can be modular (e.g., engine blocks, cylinder heads, and sensors are easily interchangeable).

The apparent engine cooling fan seen in Figure 2.1 was equipped with a variable opening cover for manual wall temperature control, as the engine is air-cooled. An actuator was placed for electronic control of this opening, as was done for the HCCI in Pochet's work [39].

Figure 2.1: Yanmar L100V engine representation

Engine type	Air-Cooled 4-Stroke Monocylinder
Displacement Volume	434.34 $[cm^3]$
Original compression ratio	21.2 : 1
Cylinder Bore	86.11 [mm]
Piston stroke	74.93 [mm]
Crank radius	37,5 [mm]
Connecting rod length	120,5 [mm]
Rotation speed	1500 [RPM]
Intake Valve Opening IVO	TDC (360 [CAD])
Intake Valve Closing IVC	-127 [CAD]
Exhaust Valve Opening EVO	127 [CAD]
Exhaust Valve Closing EVC	TDC (360 [CAD])

Table 2.1: Yanmar L100V specifications

For the experiments conducted by Mauro Daese, he made several modifications to the original engine design. These are explained in the following sections.

2.1.1 Piston head

Mauro Daese modified the piston head for his Ph.D. thesis. His study focuses on the combustion with any combination of air, O_2, CH_4, CO_2, and H_2. Then according to Tangöz et al. [40], the ideal CR for a natural gas/hydrogen mixture engine is around 12. Moreover, this value ensures an excellent compromise to limit knocking.

For this purpose, the deep hexagonal bowl piston (Figure 2.2) was machined into a low turbulence shallow bowl piston (Figure 2.3), reducing the CR from the original value of 21.2.

The new design of the bowl piston is represented in Figure 2.3. The reader can find a technical drawing of the top of the piston in Appendix A.6. Knowing the volume of the original hexagonal bowl and that 2.6 mm were ground off the surface of the cylinder before the circular bowl was machined, it is possible to compute the new geometric CR of the set-up.

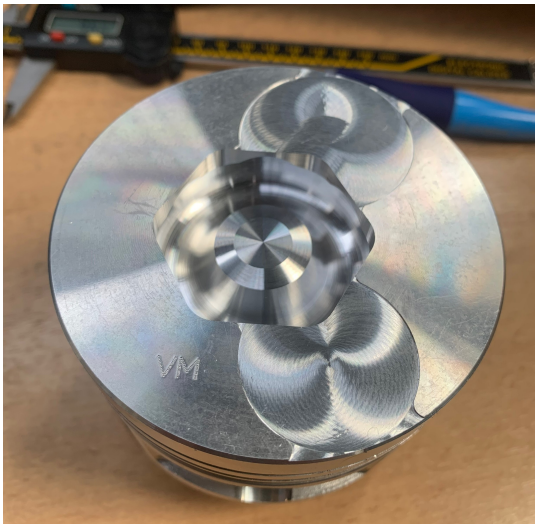

Figure 2.2: Piston head before modification.

Figure 2.3: Piston head after machining.

Bowl volume	$17[cm^3]$
Hexagon side	$2.1[cm]$
Surface of the hexagon	$11.4575[cm^2]$
Hexagon shaped volume	$2.98[cm^3]$
Piston diameter	$85.4[mm]$
Head gasket thickness	$0.5[mm]$

Table 2.2: Original piston head and bowl dimensions used to compute the new geometric CR.

The new design of the bowl piston is represented in Figure 2.3. The reader can find a technical drawing of the top of the piston in Appendix A.6. Knowing the volume of the original hexagonal bowl and that $2.6[mm]$ were ground off the surface of the cylinder before the circular bowl was machined, it is possible to compute the new geometric CR of the set-up.

The differences in volume brought by the modifications are evaluated thanks to SolidWorks models and the original bowl dimensions given in Table 2.2:

- Volume difference of the "plain" piston head due to thickness ground $= 14.32 - 2.98 = 11.34[cm^3]$ (subtracting the volume of the hexagon shape that would then be counted twice otherwise).
- Volume difference between the "plain" piston head with grinding and the same piston head with grinding and the circular bowl machined $= 25.615[cm^3]$

$$CR = \frac{V_d + V_c}{V_c} \text{ with } V_d \text{ the displacement volume, } V_c \text{ the clearance volume} \quad (2.1)$$

Using Equation 2.1, the clearance volume of the original design was $V_c = 21.5[cm^3]$. By subtracting the original bowl's volume and the hexagonal volume above it, the clearance

volume left is 4.5[cm^3]. When adding the values of the volume differences found, the new clearance volume can be evaluated at $V_c = 41.455[cm^3]$ and the new geometric CR is 11.478.

2.1.2 Flywheel

The flywheel was adapted to enable the implementation of a crankshaft position sensor placed at the extremity of the crankshaft. Slots were drilled to this effect into the periphery of the flywheel, allowing the crank angle position sensor to record correctly. The data acquisition is realized through imaging scanning. The information is then fed to the Engine Control Unit (ECU), which is presented in Section 2.2.5, to allow for accurate control of the injection timing and spark timing.

2.1.3 Camshaft

As mentioned earlier, hydrogen is used in the context of this master thesis, and Mauro Daese will work with higher hydrogen amounts for his studies. Even though hydrogen has many advantages regarding combustion, as stated in Section 1.4, its low ignition energy induces abnormal combustion phenomena such as pre-ignition and backfire. Backfiring or back-ignition [41] happens when hot spots remain in the combustion chamber and ignite the fresh air-hydrogen mixture at the intake, as explained in Section 1.2.2 .

The fact that the engine runs in the high average of CR values for SI engines already helps expel the flue gases. However, Mauro Daese proposed modifying the camshaft profile to adapt the valve timing for safer operation.
Advancing intake valve timing would increase the volumetric efficiency. Although, this enhances the possibility of backfiring to occur. Late closing of the intake valve can also induce backfiring after fuels build up next to the valves [42]. A compromise has then to be found, hence the camshaft modifications. Lee et al. [43, 44] established that the best intake valve opening timing strategy to get rid of backfire is TDC. Moreover, reducing the valve overlap period decreases the possibility for exhaust gases to cause ignition in the intake manifold.

The IVO and EVC were then both set to TDC. On the advice of the workshop which conducted the changes, Cat Cams N.V., IVC, and EVO timings were kept standard to avoid significant losses in volumetric efficiency. The final effective timings are displayed on Table 2.3.

Valve	Opening	Closing
Intake	TDC	233 CAD
Exhaust	487 CAD	TDC

Table 2.3: Valve timings after modification of the camshaft lobes.

2.1.4 Cylinder head

The cylinder head was modified to add a pressure sensor, and the diesel injector was replaced with a spark plug to use the engine in SI mode. The specific cylinder head used was previously exploited by Colette and Gatin in their study on Water Direct Injection (WDI) in HCCI engines [45]. They used a clamping device to fix the direct water injector and a thread produced in the cylinder head. Additionally, the clamping device, as well as the cylinder head itself, were drilled to receive the in-cylinder pressure sensor. The thread for the injector was repurposed for the spark plug by Daese.

Baş et al. [46] studied the variation of spark plug type and spark gap with hydrogen and methanol-added gasoline fuel. Their research underlined that iridium and platinum spark plugs deliver higher power output and lower fuel consumption, as shown in Figure 2.4. The spark plug used for these experiments is the NGK SILMAR8A9S and was selected based on these research studies, the thread dimensions, and taking into account the risks of pre-ignition of methanol. The spark plug has a heating range of 8, corresponding to a cold type spark plug, as explained in Section 1.2.2.

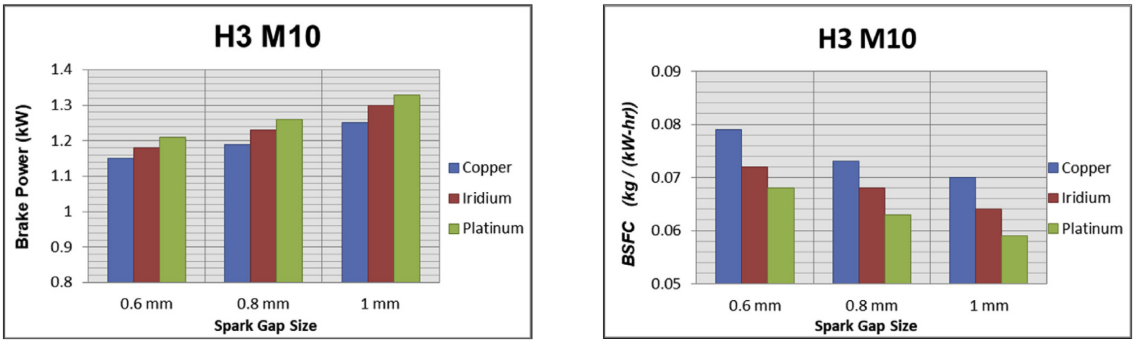

Figure 2.4: Brake Power and Brake Specific Fuel Consumption with spark plugs in Copper, Iridium and platinum, for varying gap size. Adapted from Baş et al. [46].

2.2 Test bench

This section describes the different components that form the test bench apart from the engine.

The engine is coupled with a WEG W22 IE2 55 kW three-phase induction generator, which behaves as a load and thus induces a brake torque. This electric generator can also act as a motor for the start of the engine. The Mitsubishi frequency inverter allows control of the engine rotational speed and delivers the power generated to the electrical grid.

Different Mass Flow Controllers (MFC) supply the intake with the other gases used throughout the experiments. Those gases are stored in cylinders outside of the bunker.

A MFC is a device constituted of a pipe in which two stainless steel probes are placed: an upstream heating probe and a downstream temperature probe. The power needed to maintain a constant temperature difference between these two probes allows the computation of the exact mass flow since the fluid's specific heat is known beforehand, and volume correction factors are known. The desired mass flows are input into the LabVIEW program, which sends the command to the different MFC.

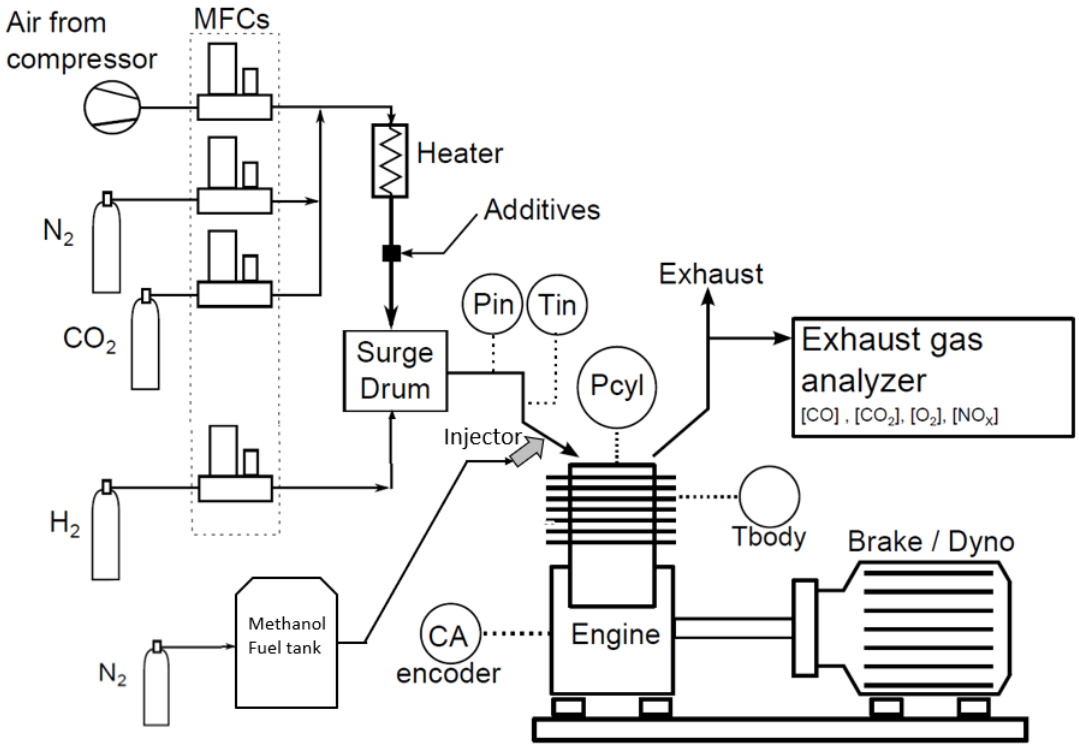

Figure 2.5: Schematic representation of the SI engine test bench.

The intake temperature and pressure are measured through sensors close to the engine's intake valve. After passing through the corresponding MFC, air passes through a 15 kW electric heater. The desired intake temperature can be fixed thanks to a PID control which adapts the heater temperature depending on the measured intake temperature. This enables accurately setting the mixture temperature before entering the combustion chamber. This feature is not used in the context of these experiments since the ambient temperature is between 25-30 °C during experiments. Therefore cold start issues are not encountered as explained in Section 1.2.2.

Interest pressures consist of the in-cylinder pressure, the intake pressure, and the exhaust pressure. These are the most important ones since they allow for studying the combustion process precisely. It also allows for the calculations of several other parameters that cannot be directly measured, such as pressure derivative, in-cylinder temperature profile, HRR, etc.

The exhaust gases are collected thanks to a flexible hose at the engine's exhaust, allowing their extraction and rejection. A portion of these gases is sampled and goes to the Horiba PG-250 exhaust gas analyzer. It can obtain a measure in ppm of the following species: NOx, SO_2, CO, CO_2, and O_2.

A summary of all the means of data recollection is given in Table 2.4.

	Quantity	Instrument	Details
Control	Engine speed	Mitsubishi inverter FR-A741	55 kW
	Intake temperature	Ohmewatt electric heater	15-200°C + PID control
	Intake mass flows	Brooks SLA585X MFCs	Air: 0-280 nL/min
			H_2: 0-55 nL/min
			CO_2: 0-15 nL/min
	Methanol injection	Bosch EV14ES (0280.158.200)	116g/min n-heptane
Slow acquisition	Intake pressure	Kistler 4260	0-5 bar
	Exhaust pressure	Kistler 4260	0-5 bar
	Intake temperature	K-type Thermocouple	0-400°C
	Body temperature	K-type Thermocouple	0-400°C
	Exhaust gas composition	Horiba PG-250	[NOx]: 0-2500 ppm
			[SO_2]: 0-3000 ppm
			[CO]: 0-5000 ppm
			[CO_2]: 0-20 vol%
			[O_2]: 0-25 vol%
	Exhaust oxygen content	Lambda sensor Bosch LSU 4.9	Lambda: 0.65 to >10
Fast acquisition	Crank angle position	Rotary encoder Heidenhain ROD 426	Resolution 0.1 CAD
	In-cylinder pressure	AVL GH15D	0-250 bar
	Charge amplifier	AVL FlexIFEM 2P2E	0-14400 pC

Table 2.4: Test bench instruments and sensors. Adapted and updated from [47, 45].

2.2.1 Fuel tank and fuel line

A fuel system generally consists of a fuel tank, a fuel pump, and an injector. Copper and its alloys are present in the fuel pump and are affected by methanol corrosion. Therefore, a simpler methodology for implementing a fuel system is conceived and is presented below.

The methanol is stored in a fuel tank at room temperature. Thus at liquid state since its boiling temperature at atmospheric pressure is 64.7°C. It is driven through 1/8" pipes thanks to the compressed nitrogen supplied by the adjacent bottle and then fed to the injector. Also, double ferrule fittings were used in the fuel line to ensure leak-free operation.

The new fuel line consists of a tank with 6 valves and two at the N_2 bottle, numbered as shown in Figure 2.6.

Figure 2.6: Fuel tank and adjacent N2 bottle.

- Valve 1 is used to pour the methanol into the tank. It is also used to pour gasoline into the tank to rinse the injector after use.
- Valve 2 is the valve through which nitrogen is supplied from the adjacent bottle. It is mounted with a pressure regulator 7 and a security flap 8. The pressure regulator allows to check the nitrogen pressure inside the bottle (0-200 bar) and set the desired pressure inside the fuel tank.
- Valve 3 is the tank's output and assures connection to the pipes running to the injector.
- Valve 4 only serves when it is needed for the tank and fuel line to be purged.
- Valve 5 is connected to Valve VA101G visible on Appendix A.1. This is security as if VA101G is shut down for emergency purposes, valve 5 closes as well.
- Valve 6 is a security relief valve that opens when the pressure inside the fuel tank exceeds 7.5 bar. It is also mounted with a manometer to check if the tank is well pressurized or depressurized.

2.2.2 Safety regarding the fuel tank and line

A safety analysis was conducted to allow the installation of the described fuel tank and line. When handling flammable products, attention has to be paid to ATEX, which stands for 'ATmosphère EXplosible', meaning explosive atmosphere. No electrical device or source can lie or be used in such zones to ensure safe operation for the installations and the people working on them. It was decided to install the methanol tank next to the existing propane bottle to reduce the ATEX zone it would create. The conducted safety analysis is found in Appendix A.3. The verification by a certified organization allowed the validation of the fuel line installation and the permit to run the engine on methanol. The ATEX zone generated is 50 cm and is shown in Appendix A.2.
Procedures for the filling and purging of the tank are explained in Appendix A.4 and A.5.

2.2.3 Injector

The chosen injector is a BOSCH EV14ES; it is a standard model which can be found in numerous mass-production cars. Its main specifications are reported in Table 2.5.

System pressure	max 5 bar (8 bar for motorsports)
Operating temperature	-40 °C to 110 °C
Maximum mass flow rate	116 g/min
Maximum volume flow rate	170 cm^3/min
Power supply	6 to 16.5 V
Resistance	12 Ohm
Fuel compatibility	Gasoline, ethanol (E85), methanol (with cleaning with gasoline)

Table 2.5: Bosch EV14ES injector specifications.

The working principle is the following: In non-operating conditions, the nozzle through which the flow is expelled is blocked by a needle maintained in a closed position by a spring. Current is sent to the electromagnet built in the injector body when the injector needs to activate, inducing the needle to rise for a short time and allowing the fuel to flow.

This particular injector is methanol compatible but requires rinsing with gasoline after use. The new tank designed for the test bench allows multiple liquid fuels to be used so that the rinsing can happen.

A mount is designed to insert the injector into the intake. It is composed of the following: a first plate that screws into a thread welded to the angle of the intake line, a second plate with a thread for connection with the methanol pipe coming from the tank (and the ferrule fitting), screws assuring the two plates are fastened correctly and that the injector is secured into the desired place. The latter parts are essential as the methanol tank is pressurized to 6 bar. The mount must be able to sustain such kind of constraints.

Design and actual mounting can be found in Figure 2.7.

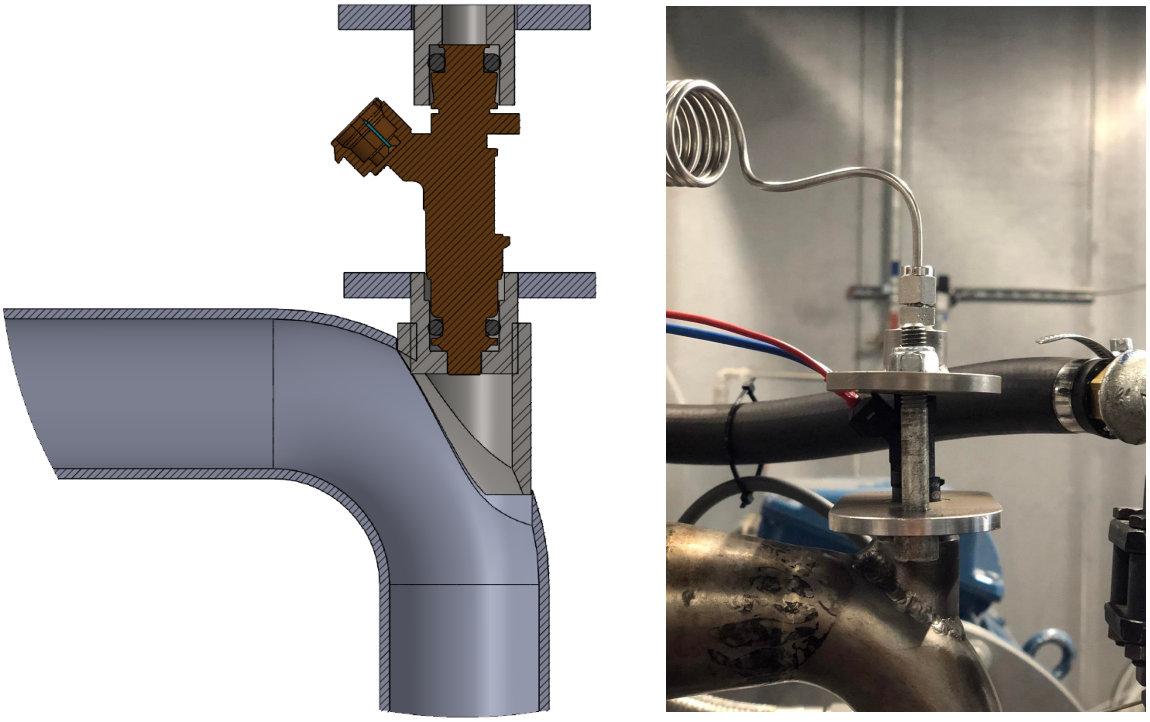

Figure 2.7: Injector mount design and implementation at the angle of the intake line.

The methanol injection system is positioned at the intake manifold elbow so that as much of the fuel flow as possible is properly mixed with the incoming airflow, thus avoiding wetting of the manifold walls, condensation, and the presence of liquid fuel in the manifold near the intake valve. In addition, this position allows easy access for calibration, flushing, and other maintenance. The injector pressure is fixed at 6 bar to enhance evaporation in the flowing air.

On the ECU, which is further introduced in Section 2.2.5, the injector is controlled by two main commands: the maximum opening time and a percentage degree on this maximum opening time. In order to assess which percentage to apply to the injector in order to obtain a precise flow during the experiments, calibration must be carried out. The latter was performed at the injection pressure. For a maximum opening time of 30 ms, the percentage was increased linearly from 0 to 100% with steps of 10%, representing opening times ranging from 0 to 30 ms with steps of 3 ms. The result of this calibration is shown in Figure 2.8. A plateau can be observed once a level of 40% or 12 ms is reached.

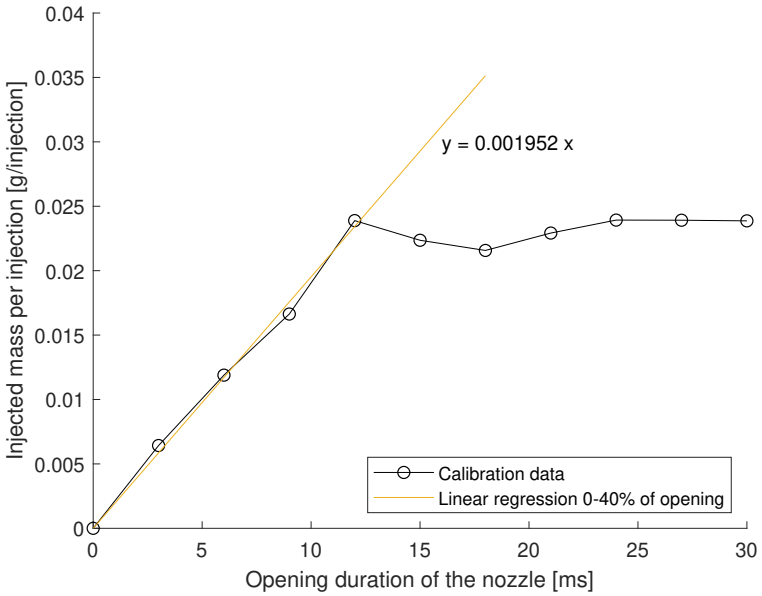

Figure 2.8: Injected mass per injection as a function of the opening duration during calibration of the injector. The linear regression is applied on the first points, namely 0, 3, 6, 9 and 12 ms of opening duration for each injection.

This behavior is unusual and is not explained by the authors. Indeed, when the injector was first calibrated, this plateau did not exist, and the curve was linear. Despite the change of injector, this behavior remains the same. Since the ECU is a complex program to handle and is still in the learning phase, it is not to rule out an error from the author in handling it, resulting in a change affecting the trends above a threshold opening duration value. Indeed, ECU contains a lot of parameters, compensations, and trims on injection, whose changes might induce limitations on the opening time. In order to keep injection reliability, it is decided to work before this plateau for the experiments, which limits the methanol quantity injected and therefore the engine power density.

Linear regression is applied to the points before the plateau, as the quantity injected is supposedly constant after 12 ms of opening time. An uncertainty analysis is conducted on the injected mass in Section 4.3.1.

2.2.4 Lambda probe

The air-fuel equivalence ratio λ is the ratio between the actual AFR and the stoichiometric one. If it is equal to one, the mixture is in stoichiometric conditions. However, if $\lambda < 1$, the mixture is rich and contains more fuel than is needed for stoichiometric operation. If $\lambda > 1$, the mixture is said to be lean.

Lambda sensors are a valuable source of information in modern-day cars as it allows the ECU to evaluate if the TWC operates properly and, if not, adapt the quantity of fuel injected accordingly. Such a device is also of fundamental importance in an experimental

installation. It is used to check that the combustion is taking place as expected and that the amount of fuel injected is close to the desired amount. The lambda sensor used in this specific test bench is a wideband λ sensor BOSCH LSU 4.9.

The sensor element in λ probes is made of zirconium dioxide ZrO_2. A ceramic heating element is placed inside the probe. The sensing element of the λ probes is made of zirconium dioxide ZrO_2. A ceramic heating element is placed inside the probe. Its purpose is to heat the λ probe in the range of 800°C to enable the zirconium oxide component to become conductive to ions.

Atmospheric air is placed inside this component, flowing through a ventilation membrane placed at the rear of the sensor [48]. If there is a difference in oxygen concentration (partial pressure) between the inside (reference gas) and the outside (exhaust gases) of the zirconium element, a difference in potential is produced, and the component acts as a Nernst cell, providing a specific voltage that is measured thanks to platinum electrodes.

The voltage is usually set at 0.450 V when the engine runs with an AFR corresponding to stoichiometric conditions ($\lambda = 1$). When the mixture is lean, the lower output of typically 0.1-0.2 V is measured as the exhaust gases contain more oxygen than at stoichiometric operation, involving a smaller difference in concentration and potential. Consequently, if the mixture is rich, a higher voltage of about 0.8-0.9 V is measured. This principle is used for narrow-band λ sensors, and its structure is represented on the left side of Figure 2.9.

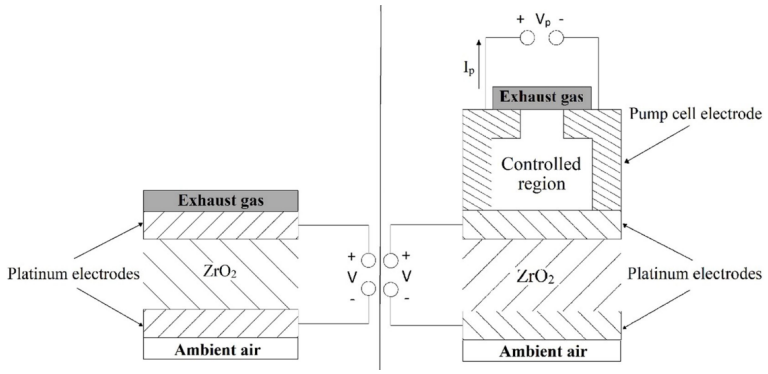

Figure 2.9: Comparison between the structure of the narrow-band and the wide-band lambda sensors, from Najjar et al. [49].

In wide-band λ sensors, a pump cell is added on the exhaust gases side as well as a monitoring chamber which makes a buffer between the two cells [48, 50]. The new architecture is represented on the right side of Figure 2.9. A diffusion gap allows the exhaust gases to enter the monitoring chamber through the pump cell. However, the composition of the gases in the monitoring chamber should always be kept at stoichiometric conditions so that the Nernst cell should always read 0.450 V. To ensure this remains the case, an electro-chemical gas pump is fed current in the pump cell, guaranteeing a specific flow of

oxygen in or out the monitoring chamber. If the mixture is lean/rich, the voltage measured at the Nernst cell is lower/higher than 0.450 V, a positive/negative current is fed to the pump cell, reducing/increasing the amount of oxygen in the monitoring chamber until $\lambda = 1$ is recovered. The current fed to the gas pump is a near linear indicator of the oxygen content in the exhaust gases, as can be observed in Figure 2.10, which was provided directly by Bosch Motorsport.

In the Bosch LSU 4.9, the concept is further improved by removing the reference air, which bad conditions around the probe could corrupt (not in laboratory conditions but happens regularly in actual life application) [51]. It is replaced by a reference pumping current, eliminating unreliable air reference.

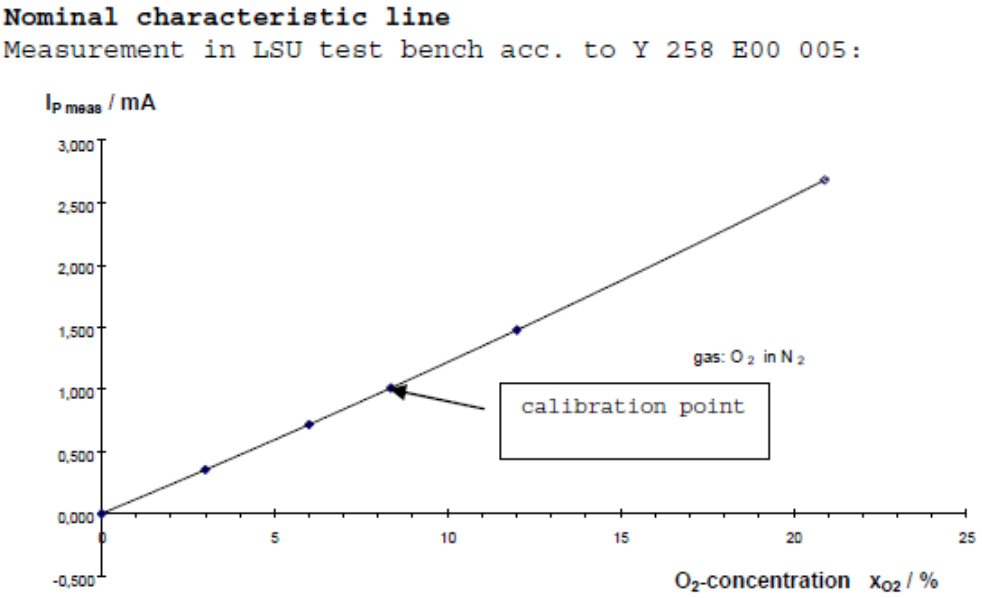

Figure 2.10: Correlation between pump current and oxygen concentration. Courtesy of Christian Dengler, Motosport Customer Account at Bosch Engineering GmbH.

2.2.5 Engine Control Unit

A MoTeC M84 Engine Control Unit (ECU) is adopted to control the spark plug and the injector. The main benefit of such configuration is excellent versatility in the use of these specific pieces of equipment. The ECU allows easy control of the following quantities through its software:

- Spark timing and combustion advance
- Injection duration
- Injection timing

The ECU is connected to the spark plug and the ignition coil, which transforms the 12 volts of electric current from the power source to 20.000 volts, allowing for optimal spark formation. The aforementioned spark timing is of great importance in determining MBT and the operating conditions of the experiments, as discussed in Section 2.3.

This device allows the injector's complete testing, calibration, and programming to be carried out efficiently. The calibration allows the mass flow rate of methanol through the injector to be determined when the injector is open. These results are beneficial when using the injector with the ECU. Indeed, the injector is controlled in the ECU by setting the injection duration, the time during which the injector opens during the cycle, inducing the desired amount of fuel to be delivered to the intake line. Also, the ECU allows controlling the injection timing, which is the CAD position at which the flow is provided. In addition to easy control of the injector parameters that regulate its output, an asset of the MoTeC M84 is that it can be wired to a lambda sensor. The ECU features the ability to handle the injector automatically to match a specific lambda given as input in closed loop control. However, this feature is not used in these experiments.

It should be noted that the ECU is configured to work with a two-stroke engine. A spark is therefore formed twice per cycle, as the Yanmar L100V is a four-stroke engine. Methanol is also injected twice per cycle, so care must be taken to inject half the fuel per cycle at each injection. One way to solve this problem would be to add a sensor to the camshaft wheel so that the ECU can sense at which time of the cycle it should inject the total amount of methanol.

2.3 Experimental procedure

This section first presents the experimental campaign conducted and then the equations used to determine the input volume and mass flow rates used for the experiments.

2.3.1 Experimental campaign

The experimental campaign is divided into three main phases. The first one consists of pure methanol combustion. The second one sees the addition of the synthetic EGR. The third and final phase is conducted with hydrogen blend. All the experiments are conducted under stoichiometric conditions. The summary is shown in Table 2.6.

Pure methanol

The first experiment is conducted with pure methanol in stoichiometric operation. The inlet pressure results from the mass flow of air brought to the cylinder and stay constant. This experiment aims to find MBT timing; An ignition timing sweep is performed between 14 to 24 BTDC. Once the MBT has been found, baseline results can be identified for the parameters of interest, allowing comparison with different levels of EGR and hydrogen enrichment. The MBT timing remains the same for the following stages of the

experimental campaign, even if, for a given EGR fraction, MBT timing probably changes. The inlet parameters remain constant throughout the procedure to properly study the effects of dilution and hydrogen blend independently of other factors.

Methanol & synthetic EGR

The second experiment consists of gradually increasing the fraction of EGR in the inlet. This synthetic EGR is added to the mixture defined in the first experiment. The objective is to analyze the combustion when the EGR fraction is increased and the EGR fraction where the combustion instability becomes too important. This instability is represented by a COV_{IMEP} around 10%. According to the literature, this fraction should be around 30% of EGR [26].

Methanol & synthetic EGR & H_2

The third experiment repeats the second experiment, but with a hydrogen/methanol blend instead of pure methanol, again under stoichiometric conditions. It is, therefore, a substitution of a part of the methanol by hydrogen. This substitution is defined in section 2.3.2 below. This third experiment aims to see the latter's impact on the combustion in the engine. Principally, the impact on the stability of the combustion is of interest. However, the impact of this blend on in-cylinder peak temperature is carefully analyzed since if increased above the pure methanol value, EGR utilization to decrease in-cylinder temperature becomes irrelevant.

Chronology	Composition	Results
First step	Pure methanol	MBT and baseline results
Second step	Methanol & synthetic EGR	Dilution limits
Third step	Methanol & synthetic EGR & hydrogen enrichment	COV_{IMEP} stabilization

Table 2.6: Experimental campaign summary.

2.3.2 Mass flows determination

The Balanced Chemical Equation (BCE) is given in Equation 2.2.

$$\begin{aligned}(n_{f1} \cdot CH_3OH + n_{f2} \cdot H_2)_{fuels} + \frac{n_{O_2 stoich}}{\phi} \cdot (O_2 + 3.76 \cdot N_2)_{air} + \alpha_{EGR} \cdot (n_{e1} \cdot CO_2 + n_{e2} \cdot N_2)_{EGR} \\ \Longrightarrow n_{p1} \cdot H_2O + n_{p2} \cdot CO_2 + n_{p3} \cdot CO + n_{p4} \cdot O_2 + \left(\frac{n_{O_2 stoich}}{\phi} \cdot 3.76 + n_{e2} \right) \cdot N_2 \quad (2.2)\end{aligned}$$

The fractions that are set for the computation of the mass flows are the molar fractions of hydrogen in the fuel blend and the mass fraction of EGR.

$$x_{H_2} = \frac{n_{H_2}}{n_{fuels}} \cdot 100\% = \frac{n_{H_2}}{n_{H_2} + n_{CH_3OH}} \cdot 100\% \quad (2.3)$$

$$\alpha_{EGR} = \frac{m_{EGR}}{m_{EGR} + m_{air}} \cdot 100\% = \frac{m_{EGR}}{m_{air} + m_{EGR}} \cdot 100\% \tag{2.4}$$

The molar fraction of methanol in the fuel mix is $x_{CH_3OH} = (1 - x_{H_2})$. It is decided to take the fraction of H_2 in molar terms because hydrogen enters a gaseous state and methanol is in a liquid state. Moreover, this definition ensures a constant ratio between the two fuels, independent of the level of dilution applied, which is of great importance when working under stoichiometric conditions. The fraction of EGR is defined in volume terms as it is extensively done in literature.

The computations of the intake parameters used for the experiments are shown in Table 2.7.

x_{H_2} \ α_{EGR}	0	5	10	15	20
0	$V_{air} = 152$ $V_{H_2} = 0$ $V_{CO_2} = 0$ $V_{N_2} = 0$ $m_{meth} = 30.2$	$V_{air} = 152$ $V_{H_2} = 0$ $V_{CO_2} = 2.7$ $V_{N_2} = 5$ $m_{meth} = 30.2$	$V_{air} = 152$ $V_{H_2} = 0$ $V_{CO_2} = 5.4$ $V_{N_2} = 10$ $m_{meth} = 30.2$	$V_{air} = 152$ $V_{H_2} = 0$ $V_{CO_2} = 8.1$ $V_{N_2} = 15$ $m_{meth} = 30.2$	$V_{air} = 152$ $V_{H_2} = 0$ $V_{CO_2} = 10.8$ $V_{N_2} = 20$ $m_{meth} = 30.2$
10	$V_{air} = 152$ $V_{H_2} = 2.5$ $V_{CO_2} = 0$ $V_{N_2} = 0$ $m_{meth} = 28.8$	$V_{air} = 152$ $V_{H_2} = 2.5$ $V_{CO_2} = 2.7$ $V_{N_2} = 5$ $m_{meth} = 28.8$	$V_{air} = 152$ $V_{H_2} = 2.5$ $V_{CO_2} = 5.4$ $V_{N_2} = 10$ $m_{meth} = 28.8$	$V_{air} = 152$ $V_{H_2} = 2.5$ $V_{CO_2} = 8.1$ $V_{N_2} = 15$ $m_{meth} = 28.8$	$V_{air} = 152$ $V_{H_2} = 2.5$ $V_{CO_2} = 10.8$ $V_{N_2} = 20$ $m_{meth} = 28.8$

Table 2.7: V_{air}, V_{H_2}, V_{CO_2}, V_{N_2} in $[Nl/min]$. m_{meth} in $[g/min]$.

The following injected quantity of fuel gives a FuelMEP of 18.2 bar while the hydrogen/methanol blend gives a FuelMEP of 17.65 bar. Therefore, for stoichiometric conditions, the energy input is not the same eventhough the moles fuel input stay contant.

Chapter 3

Processing of experimental data

This chapter first presents the methodologies used to calibrate the engine against experimental data. The calibration results are then presented, and a sensitivity analysis is performed on the influence of calibration parameters on the CHR (CHR). The second part of the chapter explains and derives the methods used to obtain the combustion parameters of interest. To properly introduce the chapter, the processing methodology is first explained

Analyzing the in-cylinder pressure measurements allows the measured quantities to be converted into the desired outputs, as it can be seen on figure 3.1.

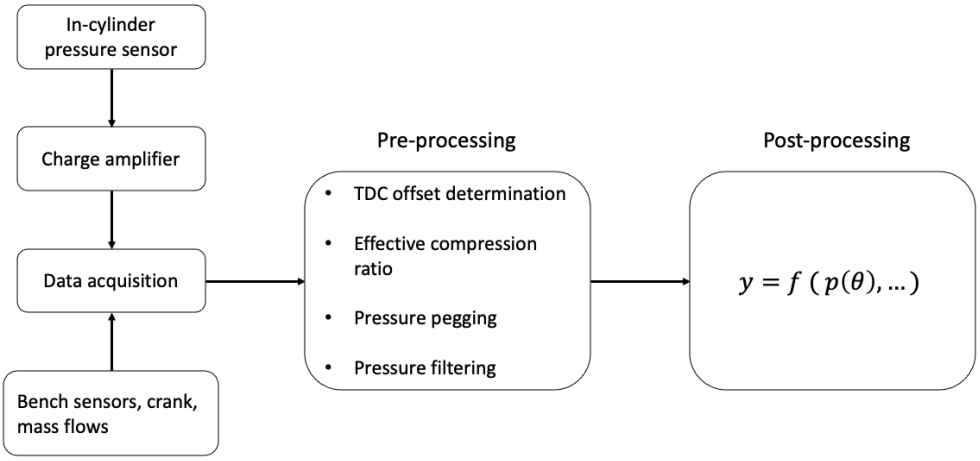

Figure 3.1: Chain processing to go from the in-cylinder pressure to post-processed quantities.

The in-cylinder pressure is converted into a current by the piezoelectric sensor, which is, in turn, amplified by the charge amplifier and sent to the recording system.

In order to use these data correctly, the experimental pressure data must be calibrated with the in-cylinder volume. Incorrect calibration of some parameters leads to errors

in estimating combustion parameters [47]. This step is particularly decisive as this is a newly implemented SI engine.

Once the data is appropriately calibrated, in-cylinder pressure data in phase with the in-cylinder volume can be used to calculate the desired combustion parameters. The calculated outputs will be determined with the pressure, volume, mass flows, and various bench sensors presented in Section 2.

3.1 Pre-processing: Calibration of experimental data

Bhaduri [47] reported the critical parameters that must be calibrated against the experimental data and are listed below:

- TDC offset determination
- Effective compression ratio
- Pressure filtering
- Pressure pegging

The latter showed that an error in estimating these parameters has the most significant impact on the combustion phasing parameters and the estimation of heat release and will therefore be addressed.
These calibration parameters depend on one another; e.g., once a new TDC offset is calculated, the pegging must be modified according to the shifted pressure profile. In order to achieve convergence of all these parameters, the calibration parameters are found with an iteration process.

The calibration methods used for these four factors are detailed in the following sections.

3.1.1 TDC offset determination

The TDC offset results from a misaligned rotary Crank Angle Encoder (CAE), which causes the in-cylinder pressure and volume to be out of sync with the CAE values.
Inaccuracy in TDC determination, causing erroneous alignment of CAD and measured in-cylinder pressure, must be eliminated for precise calculation of combustion parameters. When mounting a CAE, the exact determination of the trigger mark relative to the actual crankshaft position is usually impossible, and the crank angle joint displacement can cause inaccuracy. It is even more valid considering that the motored curve on the SI test bench shows a peak pressure of 10 CAD ATDC, indicating the inaccuracy of the phasing and the need for calibration.
Therefore, a method is needed to measure and correctly set the trigger mark's position to the absolute crankshaft position. Ideally, the peak pressure position should be at TDC under motoring conditions. However, due to wall heat transfer, the peak pressure

is ahead of TDC under actual engine operating conditions. The difference between the actual TDC and the crank positions corresponding to the peak pressure at TDC is defined as the thermodynamic loss angle.

The loss function method for determining TDC offset is proposed by Pipitone et al. [52] and is the procedure employed. It accounts for the heat transfer influence of the cylinder as well as mass leakage. It estimates the TDC position by introducing the notion of a loss function δF shown in Equation 3.1.

$$\delta F = Cp\frac{\delta V}{V} + Cv\frac{\delta P}{P} \tag{3.1}$$

Where Cp and Cv are the gas specific heat at constant pressure, and constant volume, respectively, and p and V are the in-cylinder pressure and volume.

Pipitone found that the loss function is not significantly influenced by the heat loss angle for a crank position near ±30CA around TDC but depends only on the engine geometry. Therefore, the loss function at the peak pressure location can be related to the angular positions θ_1 and θ_2 of the minimum and maximum $\delta V/V$, where angular positions are calculated with the following Equation 3.2 where β is the rod stroke ratio and CR is the engine Compression Ratio.

$$\theta_{1,2} = \pm 76.307\beta^{0.123}\tau^{-0.466} \tag{3.2}$$

The relationship between these two loss functions evaluated at these two positions can be derived using Equation 3.1 and is averaged. Then, the loss function at the maximum pressure position can be evaluated with Equation 3.3.

$$\delta F = 1.95\delta F_{mean} \tag{3.3}$$

Finally, the loss angle θ_{loss}, and, thus, the TDC position is found using Equation 3.4.

$$\theta_{loss} = 2 \tag{3.4}$$

The resulting TDC offset determination can be seen in Figure 3.2. The loss angle is negative, as expected, because of the heat transfer at the wall, and therefore, the peak pressure is reached before reaching TDC.

3.1.2 Effective compression ratio

The computation of the in-cylinder volume is affected directly by the engine's CR, which depends on the displacement volume and the clearance volume. The displacement volume is given in the engine data sheet and is a reliable specification as it depends on the kinematics of the connecting rod. The determination of the clearance volume is more challenging as it involves the crevices formed by the first piston ring and the cylinder, the crown region between the piston, the head gaskets, the spark plug thread, the valve seat gaps, etc., which are not taken into account in the calculation of the clearance volume.

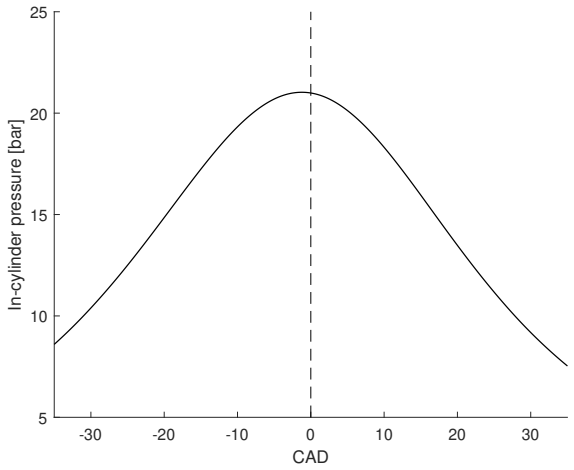

Figure 3.2: Loss angle shown for motoring in-cylinder pressure.

Furthermore, in the context of the experiment, the combustion chamber has a potentially more significant clearance volume depending on the instruments used, such as an in-cylinder pressure sensor on the test bench in the present case. Due to geometrical uncertainties, the geometrical CR may diverge from the actual one.

Moreover, the effective CR diverges from the geometrical one. Indeed, it depends on the other engine parameters, such as the valve timing, which influences the time at which compression in the engine actually starts. This is because once the engine runs, the gas trapped in the cylinder is only influenced by the effective CR due to delayed IVC, blow-by, or other volume flaws that cannot be gauged. Therefore, for thermodynamic aspects such as heat release analysis, the CR to use in Equation 3.9 is the effective ratio [39].

The precise value of the effective CR is crucial as it influences the cylinder volume, the estimation of the Rate of Heat Release (RoHR), and, consequently, the engine performance. Therefore, an alternative procedure for determining the CR using in-cylinder pressure measurement is used.

The method used is based on a motoring pressure curve. Since no heat release takes place in such, it implies that the CHR should be zero throughout the cycle as this only compensates for the heat losses in the cylinder. Therefore, the RoHR is computed with Equation 3.34 for different CRs, starting from the original estimated 11.5. Using the least squares method, the RoHR closest to zero gives the effective CR. The obtained effective geometrical CR is 9.8 .

3.1.3 Pressure filtering

Accurate measurement of in-cylinder pressure is necessary to obtain quality data and its subsequent processing. Most of the information on the combustion process is generated

by post-processing the cylinder pressure signal. It is, therefore, of utmost necessity to obtain accurate physical information exempt from noise signals. In order to preserve the physical information in the signal pressure, it is necessary to discard the high-frequency noise. As signal differentiation results in increased noise, filtering the cylinder pressure signal is essential. For example, the heat release calculation uses pressure derivatives, leading to a significant error in calculating the heat release. Averaging the cylinder pressure data over several cycles to reduce pressure processing errors can only remove the random noise from the pressure signal, not the systematic errors. Filtering out the signal noise is the only prospect in the case of systematic errors and when signal averaging cannot be performed.

The method used for filtering is the Payri method [53], which employs a low-pass filter with a Finite Impulse Response (FIR). Identifying the optimal cut-off frequency is the major problem of low-pass filters. The noise-to-signal ratio becomes significant above the cut-off frequency. In addition, direct removal of the high-frequency band can lead to an overshoot of the pressure signal (Gibbs effect), which provokes a substantial error in the heat release estimation. This effect can be eliminated by smoothing the transition with a Hanning window that is defined between two cut-off frequencies: the stop band's initial frequency and the stop band's final frequency.

The FIR step filter used is calculated using Equation 3.5 and Equation 3.6.

$$P_k^{filt} = P_k.\theta_k \tag{3.5}$$

$$\theta_k = \begin{cases} 1 & \text{if } k < k_c - \frac{k_{stop}}{2} \\ \frac{1}{2}.\left[cos\left(\frac{k-\left(k_c-\frac{k_{stop}}{2}\right)}{k_{stop}}.\pi\right)+1\right] & \text{if } k_c - \frac{k_{stop}}{2} < k < k_c + \frac{k_{stop}}{2} \\ 0 & \text{if } k < k_c + \frac{k_{stop}}{2} \end{cases} \tag{3.6}$$

where P_k is the content of the pressure signal averaged at harmonic k and P_k^{filt}. k_c is the cut-off harmonic, and k_{stop} is the edge harmonic of the stop band.

The inverse Discrete Fourier Transform (DFT) is used to obtain the mean and filtered pressure in the time domain. The cut-off harmonic is calculated as the point where the average cycle harmonics meet the non-cyclic harmonics due to signal noise and cycle-to-cycle fluctuations. For this purpose, Payri developed an adaptive method for automatically determining the cut-off frequency for cylinder pressure smoothing. This method is based on a statistical analysis of the DFT representation of the signal: the signal-to-noise ratio is identified and used to detect the frequency where the noise contribution is equal to the signal contribution. The procedure derived by Bhaduri [47] is applied.

The filtered pressure profile can be seen in the following Figure 3.3. As expected, the unfiltered pressure derivative sees the noise signal amplified significantly. It is removed when filtered.

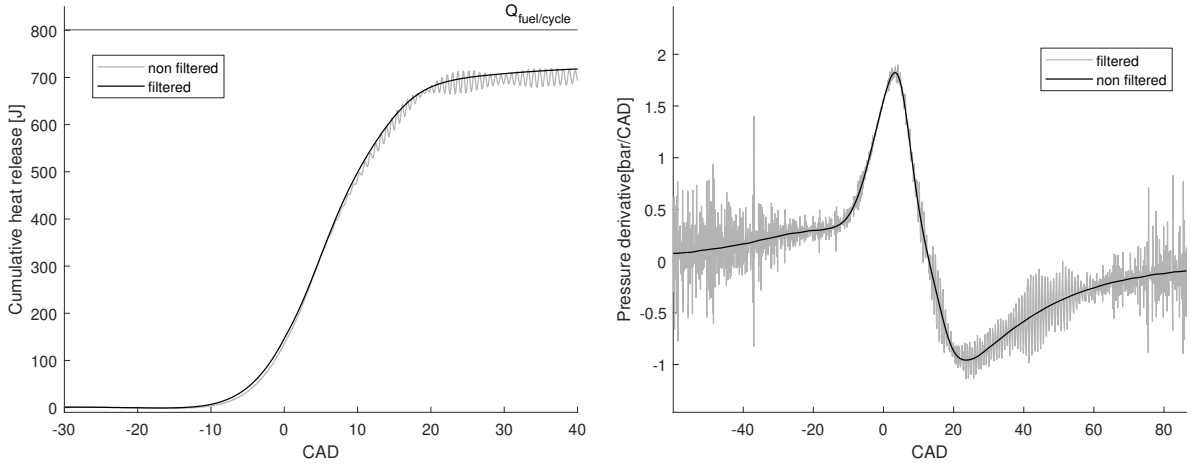

(a) In-cylinder pressure.

(b) In-cylinder pressure derivative.

Figure 3.3: Comparison between unfiltered and filtered in-cylinder pressure trace for the MBT case of stoichiometric methanol operation.

3.1.4 Pressure pegging

For each data acquisition performed, three hundred engine cycles are recorded. A piezoelectric sensor acquires the in-cylinder pressure signal, and a relative pressure is measured, meaning that only the temporal (or angular) variations are exploitable, not the absolute values. Therefore, it requires calibration to another absolute pressure variable, which is the so-called pressure pegging $\Delta_{p_{peg}}$.

Since the pegging shift is constant within each cycle but may vary between consecutive cycles [54], each cycle must be shifted according to its specific $\Delta_{p_{peg}}$. In order to compute the pressure pegging $\Delta_{p_{peg}}$, the absolute pressure sensor, which is placed just before the cylinder intake (see PID on appendix A.1) is taken as a reference. Indeed, when the intake valve is opened, both absolute and relative sensors are coordinated, and the in-cylinder pressure signal is shifted to the intake manifold pressure signal. This method is particularly effective when the engine rotational speed is low. Since the engine is running at 1500 RPM, the pressure pegging is calculated with Equation 3.7 in this region and, more precisely, at BDC, since the gas dynamics are the smallest at this piston position [39].

$$\Delta_{p_{peg}} = p_{in} p_{cyl,BDC} \tag{3.7}$$

Where p_{in} is the intake pressure sensor and $p_{cyl,BDC}$ is the measured relative pressure at BDC. The intake absolute pressure sensor is chosen because it is the sensor for which the fluctuations between the cycles are the smallest. This must be repeated for each cycle.

3.1.5 Sensitivity analysis of the calibration parameters

The sensitivity of the calibration parameters is carried out to assess the impact of an error in the calibration parameters on the CHR, computed in Section 3.2 and highlight the importance of proper calibration for the experimental results.

First, the sensitivity analysis is shown for the pressure filtering in Figure 3.4. It is observed that an unfiltered pressure signal will converge more or less to the same value. Only fluctuations are present. Filtering allows getting rid of them.

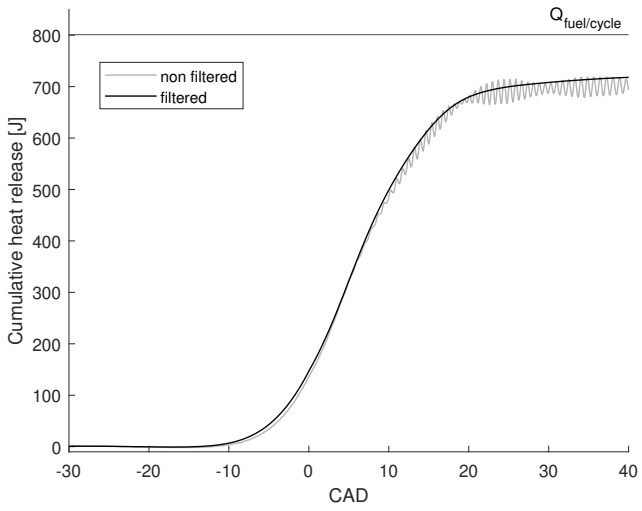

Figure 3.4: Variation of the CHR as a function of CAD when the pressure is filtered or not.

Second, the sensitivity analysis is presented for the CR in Figure 3.5. It can be seen that an overestimation of the effective CR leads to an underestimation of the CHR. In contrast, an underestimation leads to overestimating the CHR.

Finally, the sensitivity analysis is presented for the pegging offset in Figure 3.6. It can be seen that poor pegging induces errors, underlining the importance of correctly transforming the relative signal into absolute.
After the experimental data calibration, post-processing is performed. The methodologies, equations, and assumptions for obtaining the combustion parameters are explained in the following section.

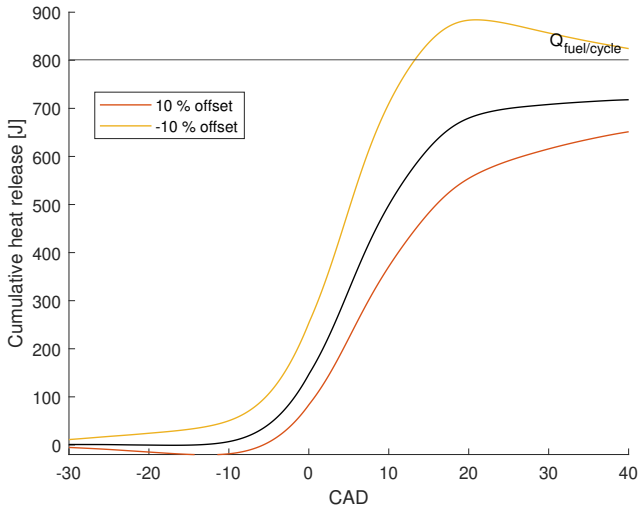

Figure 3.5: Variation of the CHR as a function of CAD when varying the CR.

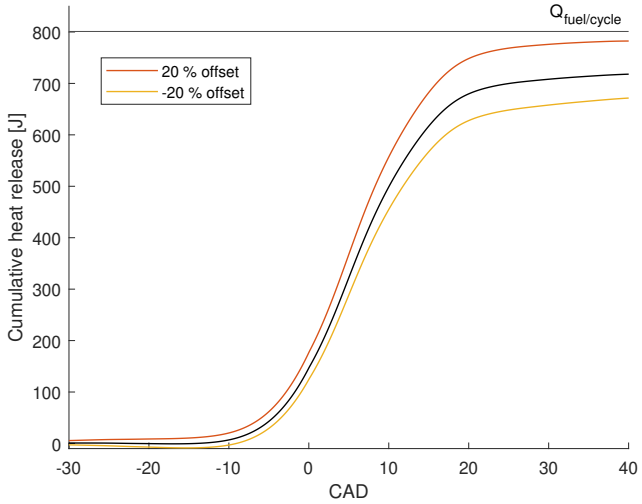

Figure 3.6: Variation of the CHR as a function of CAD when varying the pegging.

3.2 Post-processing of experimental data

In the frame of this master thesis, the output of interests are the following:

- Performances and efficiencies evaluated through IMEP.
- Combustion duration evaluated through RoHR, CHR and their resulting parameters.

In the following sections, the path from measured values to the values of interest is explained. First, are derived the expressions which enables to go to desired values.

3.2.1 In-cylinder volume

The combustion chamber is considered as a cylinder. The cylinder volume V is described by the kinematics of a connecting rod-crank system in Equation 3.8. The volume can be calculated with Equation 3.9.

$$z(\theta) = r\left[1 - cos(\theta) + (\lambda) - \sqrt{(\lambda)^2 - sin^2(\theta)}\right] \tag{3.8}$$

$$V(\theta) = \frac{V_c}{\tau - 1} + \frac{V_c}{2}\left(\lambda + 1 - cos(\theta)\sqrt{\lambda^2 - \sin^2(\theta)}\right) \tag{3.9}$$

where

- V_c is the cylinder volume at BDC
- τ is the CR and is the effective for thermodynamic calculations
- $\lambda = \frac{L}{r}$ is the ratio between the connecting rod length and the crank radius, not to be confused with the air-fuel equivalence ratio

Its derivative can be calculated with the following Equation 3.10.

$$\frac{dV}{d\theta} = V_c\frac{\sin\theta}{2}\left(1 + \frac{cos\theta}{\sqrt{\lambda^2 - sin^2\theta}}\right) \tag{3.10}$$

3.2.2 In-cylinder temperature

The in-cylinder temperature can be computed through the ideal gas law with the following Equation 3.11.

$$T(\theta) = \frac{p(\theta)V(\theta)}{Rn_{cyl}} \tag{3.11}$$

Since there is no positive valve overlap and the blow-by effect is neglected, it is fair to assume that the in-cylinder mass is constant during combustion between the IVC and EVO. Hence, the temperature can be calculated with the following Equation 3.12.

$$T(\theta) = p(\theta)V(\theta)\frac{M_m(\theta)}{m_{IVC} \cdot R} \tag{3.12}$$

Here the assumption is made that the molar mass follows the combustion rate and therefore is a function of the molar mass at IVC, products and the Mass Burned Fraction (MBF). Also, it is assumed that all the product species are formed at the same rate, as shown in Equation 3.13.

$$M_m(\theta) = M_{m,IVC} \cdot MBF + M_{m,prod} \cdot (1 - MBF) \tag{3.13}$$

Solving the ideal gas law for the mass in the cylinder requires information on the temperature during compression or expansion. However, temperature measurements in the cylinder are complex and may not be accurate enough. Accurate temperature measurement is crucial because any deviation from the actual temperature will result in an error in trapped gas mass calculation. It is thus of interest to use an approach to establish the amount of trapped gas mass to determine the temperature throughout the cycle properly.

Residual Gas Mass

It is assumed that the exhaust gas temperature propagates from the engine cylinder to the exhaust manifold so that the temperature at the EVC equals the temperature in the exhaust manifold. The residual gas mass can be determined from Equation 3.14.

$$n_{EVC} = \frac{p_{EVC} V_{EVC}}{R T_{em}} \tag{3.14}$$

Where T_{em} refers to the measured exhaust manifold temperature.

However, the exhaust manifold pressure differs from the cylinder gas pressure at the instant EVC. This implies that the above assumption requires to be modified in order to more accurately predict the residual gas mass. The temperature at EVC can be calculated with the following Equation 3.15.

$$T_{EVC} = T_{em} \left(\frac{p_{em}}{p_{EVC}} \right)^{\frac{1-\gamma}{\gamma}} \tag{3.15}$$

Where γ is the specific heat ratio of the burnt gas at EVC. Since this temperature is unknown yet, γ can be approximated to the temperature of the exhaust manifold for the primary guess. In order to avoid adding an assumption during the calculation steps, an iteration is performed to adjust γ at the temperature at EVC until convergence is reached. γ is calculated as explained in Section 3.2.4 with Equation 3.40, making the rational assumption that the fraction of gas burnt at the EVC is 1.

The iteration follows the iteration scheme in Figure 3.7.
This first step of calculations allows calculating T_{EVC}, the corresponding γ, and the value of the residual gas mass.

Total In-Cylinder Trapped Gas Mass

With the residual gas mass being determined, the temperature at IVC can be calculated by considering the total in-cylinder trapped gas mass.

When the intake valve opens, mixing between the intake gases and the residual gases, as well as the heat transfer between the mixture and the combustion chamber walls, take

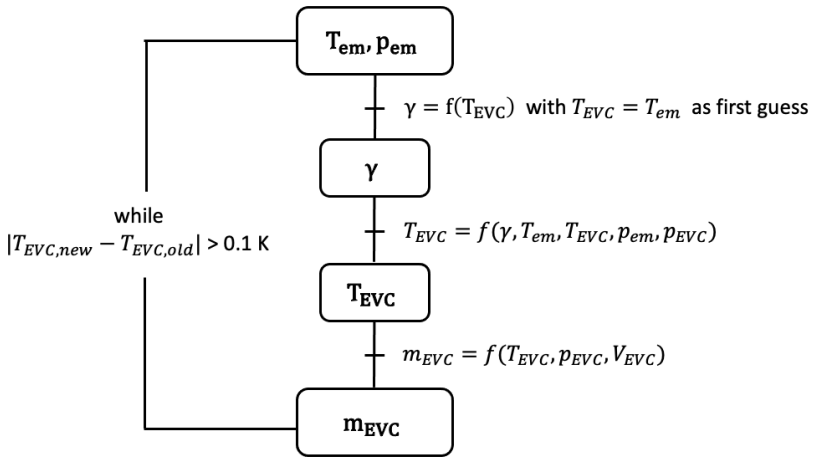

Figure 3.7: Iteration scheme for determination of residual gas mass.

place.

In order to simplify the approach, the assumption that all mixing takes place at IVC has been made. At this point, and since there is no positive valve overlap, the following energy balance can be written as in Equation 3.16.

$$m_{IVC}c_{v,IVC}T_{IVC} = m_{im}c_{v,im}T_{im} + m_{EVC}c_{v,EVC}T_{EVC} \tag{3.16}$$

Where T_{air} and T_{res} are the temperatures after the wall heat transfer is completed and are challenging to quantify. Hence, the assumption is that these temperatures are the temperature at the intake manifold and EVC. As the heat transfer at the inlet is negligible compared to the heat transfer when combustion occurs, this method is less accurate and gives results that slightly underestimate the temperature.

As the purpose is to compute T_{IVC} from the energy balance of Equation 3.16, each side of this Equation can be divided by $m_{IVC}c_{v,IVC}$. Also, the inlet air mixture can be substituted by the expression in Equation 3.17.

$$m_{air} = m_{IVC} - m_{EVC} \tag{3.17}$$

As mentioned in Section 3.2.2, the residual gases are solely composed of burnt gases, as the experimental runs are done at stoichiometric conditions. Therefore, the inlet air mass represents the entire fresh charge entering the cylinder during the intake stroke.

m_{IVC} can finally be calculated with the perfect gas law as in Equation 3.18.

$$m_{IVC} = \frac{p_{IVC}V_{IVC}}{R_{IVC}T_{IVC}} \tag{3.18}$$

By including Equation 3.17 and 3.18 in Equation 3.16, the final expression for the temperature at IVC can be derived as shown in Equation 3.19.

$$T_{IVC} = T_{air}\frac{c_{v,air}}{c_{v,IVC}} + \frac{m_{EVC}R_{IVC}T_{IVC}}{p_{IVC}V_{IVC}}\left(\frac{c_{v,res}T_{res}}{c_{v,IVC}} - \frac{c_{v,air}T_{air}}{c_{v,IVC}}\right) \tag{3.19}$$

As can be seen, the expression to find T_{IVC} contains T_{IVC} and therefore is an iterative process to get the actual temperature. To find the first value of T_{IVC}, it consists in first finding the mass in the cylinder at IVC, determining a first guessed temperature at IVC, and then finding the updated value of m_{IVC} using the Δp method as described by [55]. This process is repeated until the mass of the cylinder converges. The iterative process can be shown in Figure 3.8.

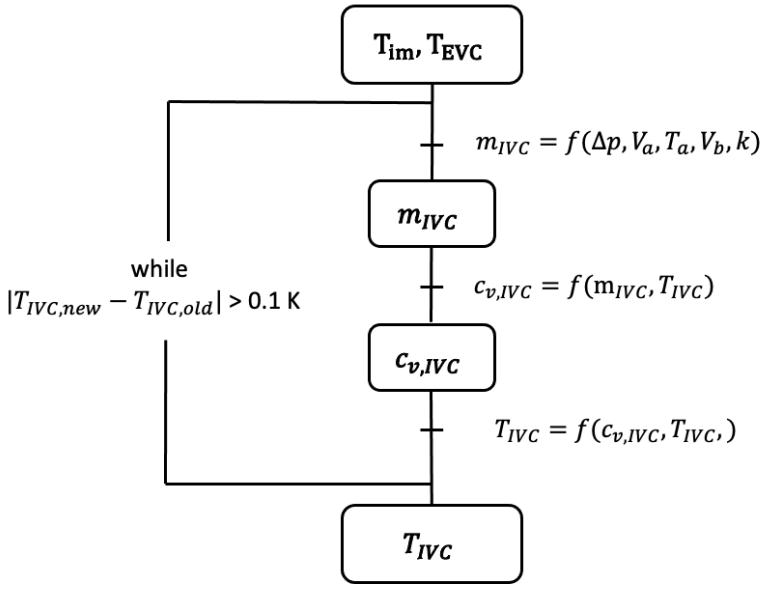

Figure 3.8: Iteration scheme for determination of m_{IVC} and T_{IVC}.

The mass in the cylinder can first be expressed as a function of the temperature of the intake manifold as shown by Equation 3.20.

$$m_{IVC} = \frac{p_{IVC}V_{IVC}}{R_{im}T_{im}} \tag{3.20}$$

A first guess can be made regarding IVC's temperature value with the computed mass. Considering an average of the temperatures at the intake manifold and at the EVC, the fraction of residual gas to the total mass is determined as shown in Equation 3.21.

$$T_{IVC} = T_{im}(1 - x_{IVC}) + T_{EVC}x_{IVC} \tag{3.21}$$

This temperature can now be used in the Δp method to obtain the total actualized mass in the cylinder. Finally, the fresh mass can be determined using Equation 3.17 and is used to determine $c_{v,IVC}$ in the iterations. The interval [a,b] chosen for the Δp method is [90 BTDC,70 BTDC] [55]. Therefore m_{IVC} can be calculated with Equation 3.22.

$$m_{IVC} = \frac{\Delta p V_a}{R T_a} \left(\left(\frac{V_a}{V_b} \right)^k \right)^{-1} \tag{3.22}$$

In order to calculate T_a, the following Equation 3.23 can be used.

$$T_a = T_{IVC} \left(\frac{V_{IVC}}{V_a} \right)^{k-1} \tag{3.23}$$

It is necessary to determine the polytropic coefficient k for the determined interval to compute Equation 3.22. For this purpose, the polytropic relationship between the in-cylinder pressure and volume in the given interval is used, as shown in Equation 3.24.

$$pV^k = C \tag{3.24}$$

By taking the logarithm of both sides of the equation, one can arrive at this Equation 3.25.

$$log(p) + k \cdot log(V) = log(C) \tag{3.25}$$

And that can be solved by an equivalent as shows Equation 3.26.

$$A \cdot x = b \tag{3.26}$$

Where x is the following vector

$$\begin{bmatrix} k \\ log(C) \end{bmatrix}$$

This allows finding the polytropic coefficient k. This method is repeated until convergence of T_{IVC}.

Since the mass is known, lastly MBF must be computed in order to calculate in-cylinder temperature. This involves an iteration on several parameters as explained in Section 3.2.4.

3.2.3 IMEP and IE

The instantaneous torque Tq that the cylinder and crank mechanism produces on the crank shaft can now be calculated. With the pressure, piston area A and lever arm l, the gas pressure torque is expressed by Equation 3.27.

$$Tq(\theta) = (p(\theta) - p_0) A \cdot l(\theta) = (p(\theta) - p_0) \frac{dV(\theta)}{d\theta} \tag{3.27}$$

where p_0 is the crank case pressure, A is the piston area and l is the lever arm.

Indicated work represents the work per cycle that the gas exerts on the piston in the cylinder. Net indicated work is calculated, for a cylinder, by taking the integral of the pressure over the variation in volume of the compression-expansion stroke while gross indicated work is over the whole cycle. These two terms are linked by the pumping work

as can be seen Equation 3.28.

$$\oint_{cycle} p(\theta)\frac{dV(\theta)}{d\theta} = \oint_{comp-exp} p(\theta)\frac{dV(\theta)}{d\theta} + \oint_{in-exh} p(\theta)\frac{dV(\theta)}{d\theta} \qquad (3.28)$$
$$W_{ind,gross} = W_{ind,net} + W_{pump}$$

where the crank case distribution disappeared when integrated over a whole cycle.

Finally, the above quantities can be turned in Mean Effective Pressure (MEP) quantities by dividing the indicated work with the displacement volume V_d.

$$IMEP_{gross} = IMEP_{net} + PMEP \qquad (3.29)$$

Since $IMEP_{net}$ represents the actual work produced by the engine, it is referred as IMEP in the following sections.

The net IE is obtained dividing the indicated work by the energy brought to the cylinder per cycle and is computed with Equation 3.30.

$$IE = \frac{W_{ind,net}}{\dot{m}_{cycle} LHV} \qquad (3.30)$$

Cyclic variation of IMEP

The intensity of cyclic variability is defined with the COV_{IMEP}. This coefficient is defined from a group of N consecutive cycles and is calculated as follows: the standard deviation of the IMEP of n consecutive cycles, divided by the mean of the IMEP of the same group of n cycles and is expressed in Equation 3.31.

$$COV_{IMEP} = 100.\frac{\sigma_{IMEP}}{\overline{IMEP}} \qquad (3.31)$$

3.2.4 Heat release

In this section are derived the expressions to characterize the combustion from a heat release point of view. The gases are assumed to behave as ideal gases.
According to the first principle of thermodynamics, the internal energy of the gases in the cylinder can be obtained as Equation 3.32.

$$\frac{dU}{d\theta} = m_{cyl} c_v \frac{dT_{cyl}}{d\theta} = \frac{dQ_{net}}{d\theta} + \frac{dW}{d\theta} = \frac{dQ_{net}}{d\theta} - p_{cyl}\frac{dV_{cyl}}{d\theta} \qquad (3.32)$$

where

- T_{cyl} the in-cylinder average temperature
- m_{cyl} the mass in the combustion chamber

- c_v the massic heat capacity at constant volume
- Q the apparent heat of combustion
- W the the work supplied to the gas in the combustion chamber

Using the ideal gas law enables to derive Equation 3.32 to obtain Equation 3.33.

$$\frac{dQ_{net}}{d\theta} = \frac{\gamma_{cyl}}{\gamma_{cyl}-1} p_{cyl} \frac{dV_{cyl}}{d\theta} + \frac{1}{\gamma_{cyl}-1} V_{cyl} \frac{dP_{cyl}}{d\theta} \tag{3.33}$$

where γ_{cyl} is the specific heat ratio of the gases in the combustion chamber, which is a function of the temperature and composition of the gases as explained below. Similarly, this gas composition depends on the degree of combustion progress, which is itself determined using γ_{cyl}. The calculation is therefore iterative.

To obtain the heat release by combustion Q_{gross}, the heat lost at the walls are added to the apparent heat of combustion and is defined in the Section 3.2.4. The final expression of the RoHR is given in Equation 3.34.

$$\frac{dQgross}{d\theta} = \frac{\gamma_{cyl}}{\gamma_{cyl}-1} p_{cyl} \frac{dV_{cyl}}{d\theta} + \frac{1}{\gamma_{cyl}-1} V_{cyl} \frac{dP_{cyl}}{d\theta} + \frac{dQ_{loss}}{d\theta} \tag{3.34}$$

Heat losses

The heat losses are assumed to only come from the convective heat transfer between the in-cylinder gases and the walls and can be calculated with the following Equation 3.35.

$$\frac{dQ_{loss}}{d\theta} = h_c S (T_{cyl} - T_{wall}) \frac{1}{\omega} \tag{3.35}$$

where

- Q_{losses} is the heat lost the wall
- h_c is the heat transfer coefficient
- S is the exchange surface between the gases and the walls
- T_{wall} is the wall temperature

The wall temperature is measured thanks to a thermocouple sensor placed at the bottom of the cylinder. Regarding the heat transfer coefficient h_c, the Hohenberg correlation is used and can be written as following Equation 3.36.

$$h_{Hohenberg} = \alpha_{scaling} V^{-0.06} p^{0.8} T_{cyl}^{-0.4} (S_p + 1.4)^{0.8} \tag{3.36}$$

where the scaling factor $\alpha_{scaling}$ is fixed at 130 , a common value for SI engines[47]

Lastly the heat exchange surface S can be computed with the following equation 3.37.

$$S = \frac{\pi D^2}{2} + \pi D R (1 - cos(\theta)) + \lambda \left(1 - \sqrt{\frac{1 - sin^2(\theta)}{\lambda^2}} \right) \tag{3.37}$$

Specific heat ratio

The ratio of specific heats are dependent on the composition and the temperature of the mixture. As the composition and the temperature of the mixture change during a cycle, it is necessary to calculate it through the whole cycle.
The in-cylinder heat capacity as a function of the cranking angle can be retrieved from the Mass Burned Fraction (MBF) and species heat capacity as shown by Equation 3.38.

$$c_p(\theta) = (1 - MBF(\theta))\left[\sum_{i}^{reactants} c_{p_i}(\theta)x_i\right] + MBF(\theta)\left[\sum_{j}^{products} c_{p_j}(\theta)x_j\right] \tag{3.38}$$

where x_i and x_j are respectively the species fraction in the reactants and products and $c_{p_i}(\theta)$ and $c_{p_j}(\theta)$ are the associated specific heat at constant pressure which depends on the temperature for each cranking angle.

Hence, with the temperature which is computed in Equation 3.2.2, the specific heat at constant pressure of each species individually can be determined with the following Equation 3.39.

$$c_p^0(T) = R(a_1 + a_2 \cdot T + a_3 \cdot T^2 + a_4 \cdot T^3 + a_5 \cdot T^4) \tag{3.39}$$

where the coefficients according to each species are taken from the NASA database [56] and are shown in Table A.1.
Finally, once the constant pressure specific heat is computed, the specific heat ratio γ can be calculated for each cranking angle with the Equation 3.40.

$$\gamma(\theta) = \frac{c_p(\theta)}{c_p(\theta) - R} \tag{3.40}$$

Cumulative heat release and MBF

The Cumulative Heat Release (CHR) is sum of gross RoHR along CAD. This quantity is of particular interest as it is useful to determine the crank angles where 10, 50 and 90% of the mass of fuel has burned with Equation 3.41.

$$Q_x = \frac{x}{100} \cdot (Q_{gross,max} - Q_{gross,min}) \tag{3.41}$$

The crank angles denominated as CA10, CA50, CA90. They respectively account for the start of combustion (SOC), the combustion midpoint and end of combustion (EOC). Another value of interest is the combustion duration which is usually defined as $CA90 - CA10 = CA_{90-10}$.
Finally, MBF along the cycle can be computed from the CHR with Equation 3.42.

$$MBF(\theta) = \frac{Q_{gross}(\theta)}{Q_{gross,max}} \tag{3.42}$$

Iteration methology

Since the temperature, RoHR, specific heat ratio and MBF relied on each other, an iteration process is required to reach convergence of these latter parameters. An iteration scheme in Figure 3.9 shows the methodology employed.

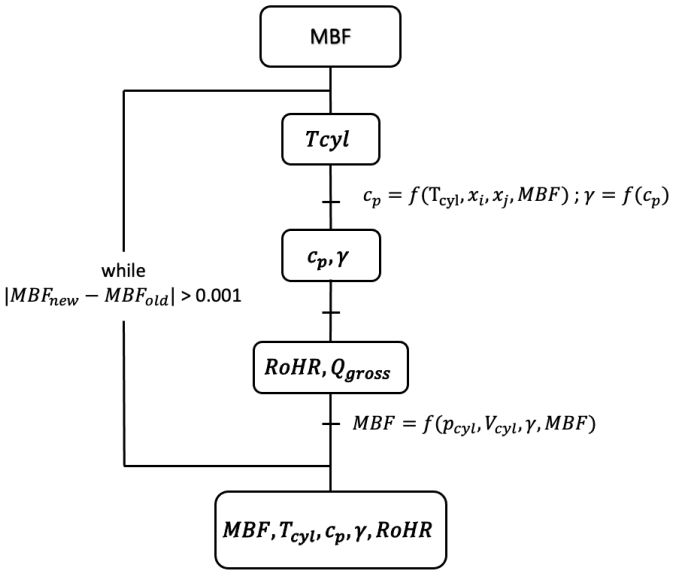

Figure 3.9: Iteration scheme for determination of γ, MBF and heat release parameters.

Chapter 4

Experimental Results

This chapter contains two main parts following the logical order of the experiments conducted. First, the results of the methanol ignition sweep are detailed. These experiments are conducted with a stoichiometric mixture of air and methanol to find the MBT timing. Second, results are presented for EGR and H_2/methanol blends. The goal is to assess the impact of H_2 blending on the cyclic variability of combustion COV_{IMEP}.

4.1 Ignition sweep

This first set of experiments aims to find the proper MBT timing. As the rotational speed is kept at a constant 1500 RPM, the friction losses FMEP can be assumed to stay constant. Therefore, BMEP, the difference between the IMEP and the FMEP, is maximum when the IMEP is maximum. The ignition sweep is conducted between 14 and 24 CAD before TDC for each 2 CAD. The higher limit is due to audible knock after 24 CAD before TDC.

Because the injector is limited in injected quantity, it results in a small intake manifold pressure $p_{im} = 0.7$ bar, inducing pumping losses. The intake manifold temperature T_{im} is kept constant even if minor variations are induced when the evaporation process is not perfect. The smallest and biggest T_{im} encountered during experiments are respectively 274.9 and 276.21 K.

4.1.1 Performances and combustion analysis

The IMEP shown in Figure 4.1, follows a weak parabolic trend with a maximum of 6.42 bar for a CAD advance of about 20 to 21 CAD. It has to be noted that the difference between IMEPs at different ignition timings remains low and that the reader should stay alert to the scale of the representation. The Indicated Efficiency (IE), shown in the same Figure, reaches 35% IE for MBT timing.
The IMEP across the ignitions sweep is relatively small. This can be explained by the fact that the engine is running with a limited quantity of fuel and thus not at full load, inducing pumping losses and an average PMEP of 0.6 bar, so a drop of around 4-5% between gross IE and IE is observed, which is relatively high. Inhomogeneities in the

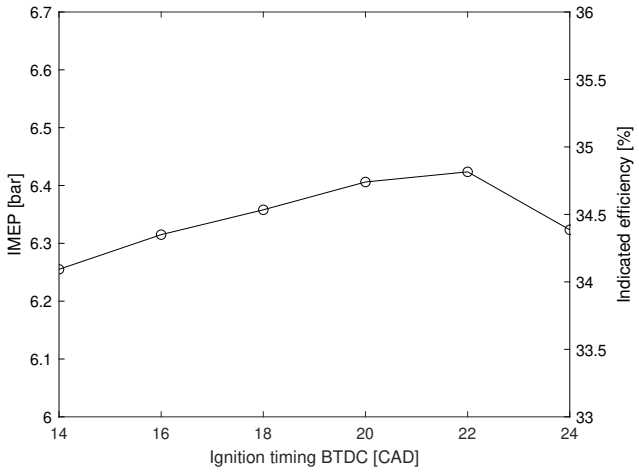

Figure 4.1: IMEP as a function of the ignition timing.

mixture because of injection happening twice per full cycle, not optimal valve timing resulting in small effective CR, and the fact that is a converted diesel engine may also play a role in this poor IE.

The influence of the ignition timing on the in-cylinder pressure is shown in Figure 4.2. As the ignition timing advances, the peak pressure point increases, and a shift towards the TDC is noticed. For a 10 CAD advance, the peak pressure is increased by an average of 5 bar, and it is shifted by 6.5 CAD towards the TDC. A net increase in the Maximum Pressure Rise Rate (MPRR) as the spark timing is advanced can be observed in Figure 4.3. MPRR values seem coherent with what can be found in the literature about SI engines [57].

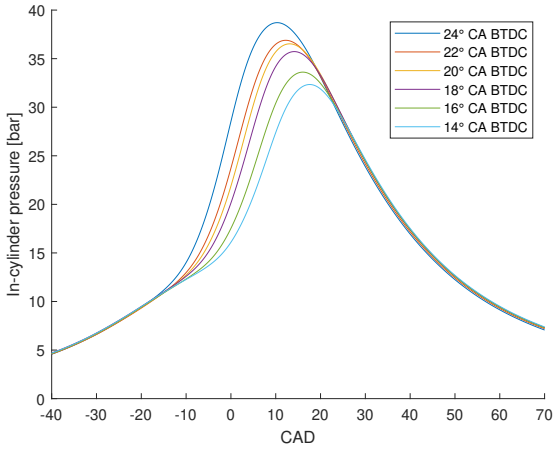

Figure 4.2: In-cylinder pressure evolution with varying ignition timing. Peak pressure increases and shifts towards the TDC.

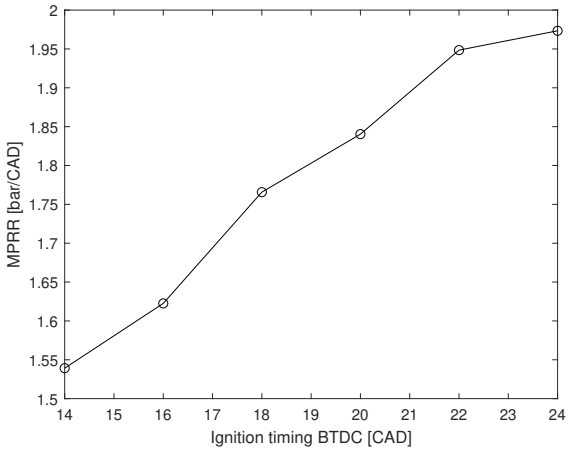

Figure 4.3: MPRR as a function of the ignition timing. Rise of about 0.5 bar/CAD for a 10 CAD ignition advance.

The RoHR follows a trend similar to the one of the in-cylinder pressure even though its representation in Figure 4.4 indicated some disordered behavior. Lou et al. [58] confirm that this trend should be verified as the phenomena are linked: fuel combustion happens at a higher rate closer to TDC, resulting in more isochoric combustion and a consequent higher pressure peak and a higher RoHR. The comparison between the CHR and the fuel energy contained in the cycle $Q_{fuel/cycle}$ on Figure 4.5 allows estimating the overall combustion efficiency (defined as the ratio between the value of the CHR at the end of the combustion and $Q_{fuel/cycle}$). It averages between 88-89%. The 24 CAD advance curve exhibits a 96% overall combustion efficiency; this point can be considered an experimental outlier.
CA50 is displayed in Figure 4.6. It follows a clear trend of 1 advance of CAD for each CAD the spark timing is increased.

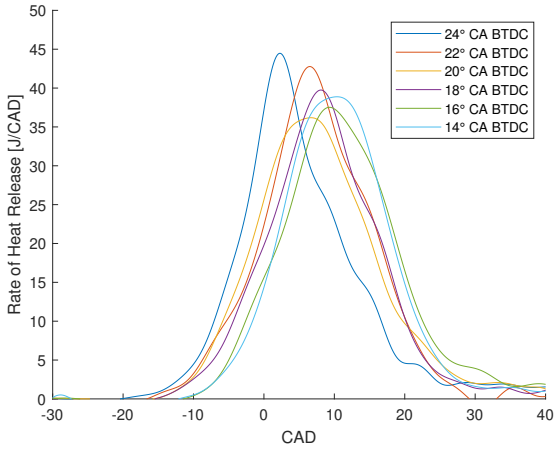

Figure 4.4: Rate of Heat Release as a function of Crank Angle Degre with varying ignition timing.

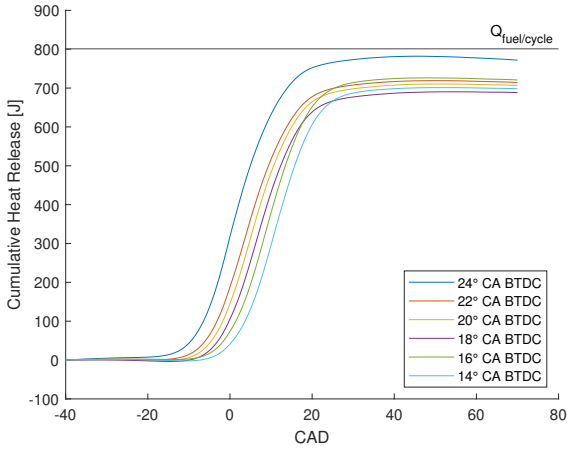

Figure 4.5: Cumulative Heat Release as a function of Crank Angle Degree with varying ignition timing.

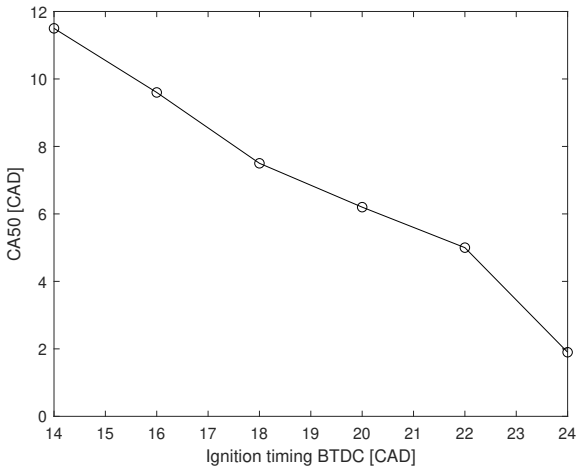

Figure 4.6: CA50 as a function of the ignition timing.

The burn duration CA_{90-10} increases by about a quarter of CAD per degree of spark advance, as is observed in Figure 4.7. This phenomenon is in line with what can be expected. Indeed, as spark timing advances, the mixture has less time to homogenize, and combustion is therefore slowed down. Ignition delay evolution is consistent with the tendency of the CA_{90-10}, Figure 4.8 displays ignition delay as a function of the ignition timing. It undergoes a slight increase when the ignition timing is advanced. This trend can be explained by the lower in-cylinder pressure and ignition temperature that induce a slower combustion start as the fire core takes more time to form itself. The last data point also lies out of this trend but is to put in perspective with the explanation given for Figure 4.5.

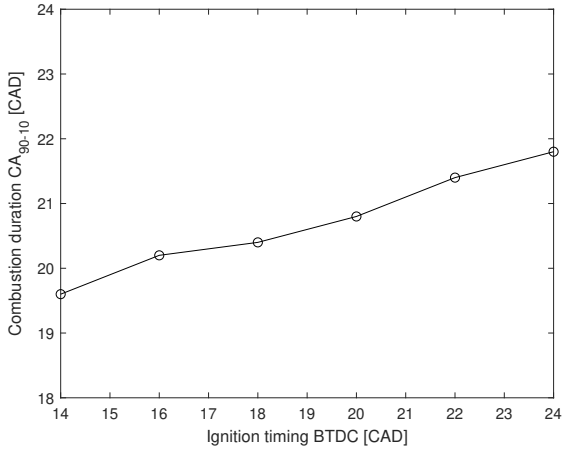

Figure 4.7: Combustion duration CA_{90-10} as a function of the ignition timing.

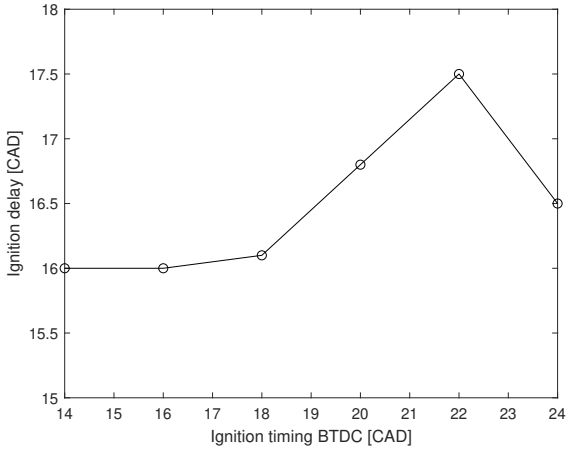

Figure 4.8: Ignition delay as a function of the ignition timing.

4.1.2 Cyclic variability

The cyclic variability, i.e., the COV_{IMEP}, is in the range of values between 3 and 4%. This value is very high compared to obtained results in the literature [26], but this has to be put in perspective. Since the modified engine used for the tests was a diesel engine in the first place, it is not designed for port fuel injection. Moreover, inhomogeneity in the intake manifold mixture, associated with inadequate valve timing, results in combustion instability. These values can therefore be considered reasonable. Here, the benefits of using methanol to reduce combustion instability in SI engines cannot be underlined since those values are already relatively high.
The purpose of this first experimental campaign is to evaluate the MBT timing through IMEP for the second part of the experiments. CA50 around 8 usually represents MBT timing. Still, the spark timing used for the second part is the one giving the maximized IMEP and is 21 before TDC. Since the second experiment is conducted under heavily diluted conditions, 21 CAD should extend the stability limits.

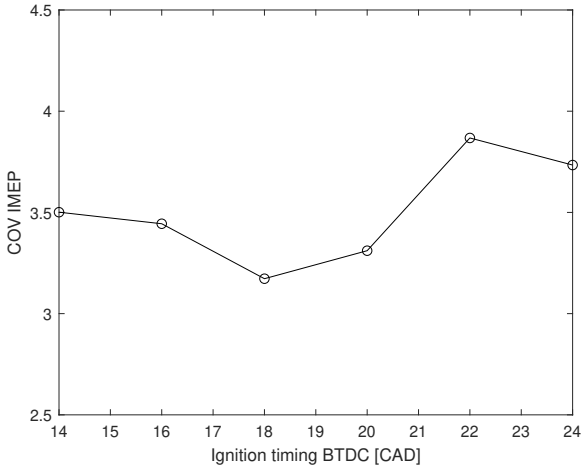

Figure 4.9: COV_{IMEP} as a function of the ignition timing.

4.2 EGR and H_2/methanol blend

This section presents the experimental results of the second and third sets simultaneously combining EGR with H_2 blend.
A discussion that alternates and compares the latter two is made. In the first section, performances are discussed and a combustion analysis is carried out. Finally, the cyclic variability is discussed.

4.2.1 Performances and combustion analysis

IMEP and indicated efficiency are the performances parameters that are assessed and are shown in Figure 4.10. IMEP of pure methanol and H_2/methanol blend increases or stays constant with the increase of EGR fraction until at first and then decreases for pure methanol. The resulting increase in IMEP is due to the reduced pumping losses, which tend to decrease as intake manifold pressure increases.

Pumping losses are still significant since EGR addition results in only a 0.1 bar increase from 0% to 20% of EGR. The positive effect of pumping losses decrease is balanced with increased EGR effect, and IMEP decreases with the growth of EGR. This may be because EGR's dilution effect results in the lowered in-cylinder temperature due to the high heat capacity of CO_2 and N_2 and that both are inert gases that do not take part in the combustion reaction. This provides a deteriorated combustion environment for the quick and complete combustion of fuel-air mixtures. Therefore, methanol combustion tends to undergo slow burning or incomplete combustion at higher EGR dilution levels, which is discussed below. On the contrary H_2/ methanol blend results in a 2% increase without EGR and a 4.5% increase with 20 % EGR compared to pure methanol.

Pumping losses are still significant since EGR addition results in only a 0.1 bar increase

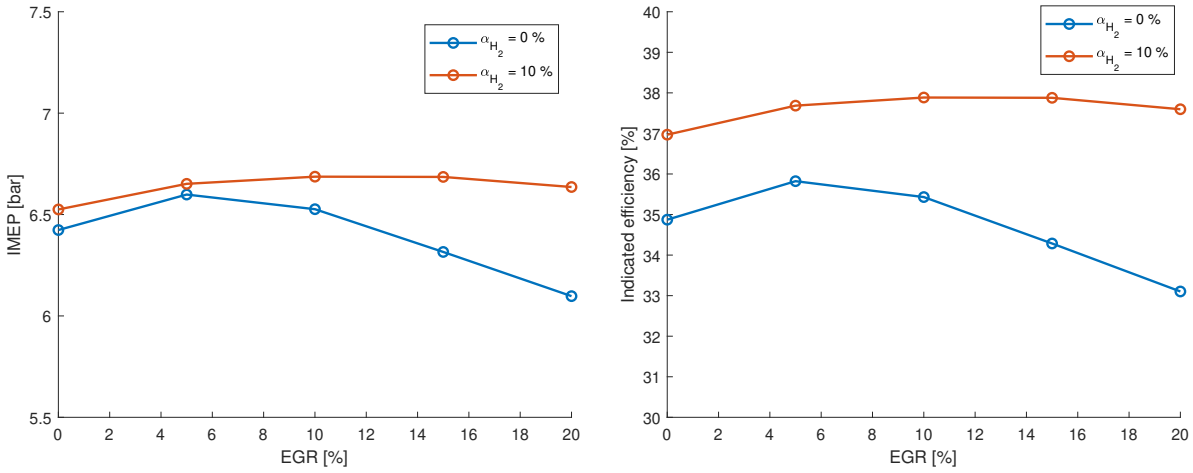

Figure 4.10: IMEP and indicated efficiencies.

from 0% to 20% of EGR. The positive effect of pumping losses decrease is balanced with increased EGR effect, and IMEP decreases with the growth of EGR. This may be because EGR's dilution effect results in the lowered in-cylinder temperature due to the high heat capacity of CO_2 and N_2 and that both are inert gases that do not take part in the combustion reaction. This provides a deteriorated combustion environment for the quick and complete combustion of fuel-air mixtures. Therefore, methanol combustion tends to undergo slow burning or incomplete combustion at higher EGR dilution levels, which is discussed below. On the contrary, H_2/ methanol blend results in a 2% increase without EGR and a 4.5% increase with 20 % EGR compared to pure methanol.

The IE increases with the H_2/methanol blend compared to the pure methanol case since the same work range is obtained but with smaller energy input. Regarding the increase of EGR fraction, since the flammability limit of H_2 is wider, the negative effect of EGR on deteriorating combustion can be overcome.

Regarding the combustion analysis, in-cylinder pressure evolution for the different percentages of EGR and for H_2/methanol blend is shown in Figure 4.11.
In both cases, when the EGR percentage rises, the peak in-cylinder pressure decreases. Furthermore, it is also observed that the latter's position is delayed when the EGR percentage is increased. However, when H_2 is introduced, these trends described above are attenuated. Indeed, when methanol is blended with H_2, the pressure peaks are higher for a given EGR percentage compared to the case without blend. This can be observed in the following Figure 4.12.
The gap between the pressure peaks becomes larger and larger as the EGR fraction increases. This difference is due to the laminar velocity of the H_2 flame, which is higher compared to methanol. Therefore, the addition of H_2 in the mixture results in faster combustion, increasing the peak pressure and resulting in a slight phase shift of position. Indeed, ignition delay as well as CA_{90-10}, which can be found in Figure 4.13, are in line with this.

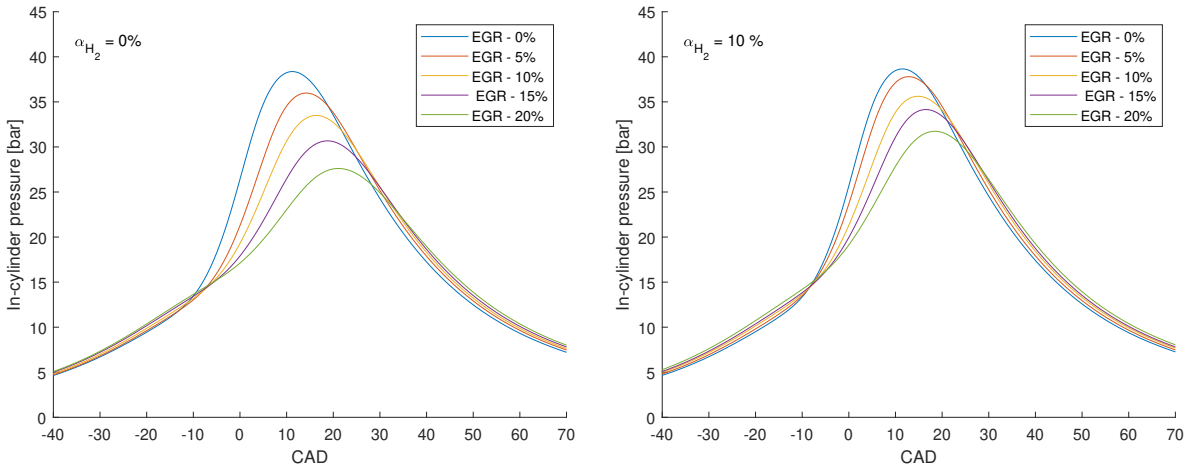

Figure 4.11: Comparison between in-cylinder with varying EGR percentage and H_2/methanol blend.

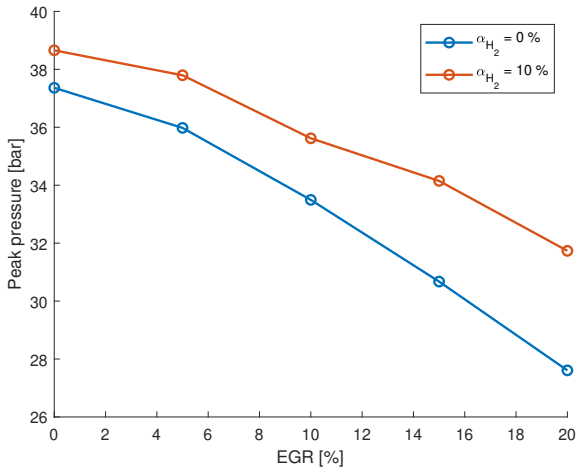

Figure 4.12: Peak in-cylinder pressure with varying EGR percentage and H_2/methanol blend.

The latter outlines the changes in the combustion development described by both the ignition delay and the burn duration. As expected, the ignition delay and CA_{90-10} increase with increasing EGR. This is due mainly to the fact that the dilution and cooling effects of increasing EGR result in a decrease in the in-cylinder temperature. As the combustion activity depends on the temperature, increasing the EGR rate increases ignition delay and CA_{90-10} in both sets of experiments. Figure 4.13 shows that H_2 blending decreases the latter parameters for a given EGR fraction and tends to attenuate EGR effects on combustion duration and ignition delay as the EGR fraction increases. Indeed, combustion duration is increased by 6.6 CAD and 3.8 CAD respectively, between 0 to 20 % EGR fraction. The reason is that H_2's broad flammability limit allows the mixture to burn

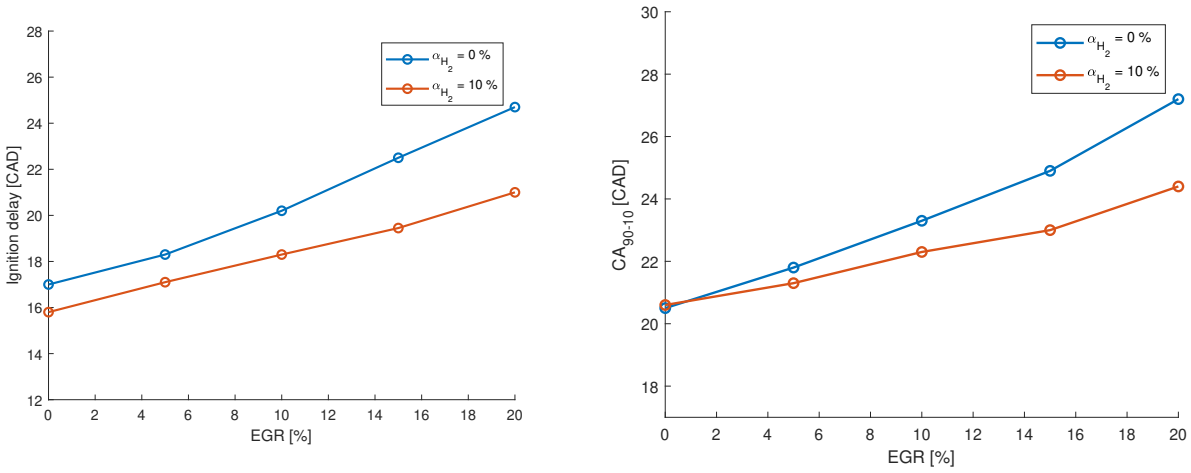

Figure 4.13: Comparison of the combustion duration with varying EGR percentage and H_2/methanol blend.

faster and more completely under dilution conditions.

Furthermore, the ignition energy of H_2 is significantly lower than that of methanol. Therefore, H_2 helps form the flame core earlier in the compression stroke. Thus, the addition of H_2 helps to reduce the ignition delay. In addition, H_2 also has a higher adiabatic flame temperature. This characteristic makes the combustion of H_2/methanol mixtures go to a higher temperature than pure methanol, as seen in Figure 4.14 below. Thus, the cooling effect of EGR on the decrease in cylinder temperature could be reduced to some extent after H_2 addition. A comment can also be made on the CA50, shown in Figure 4.14.

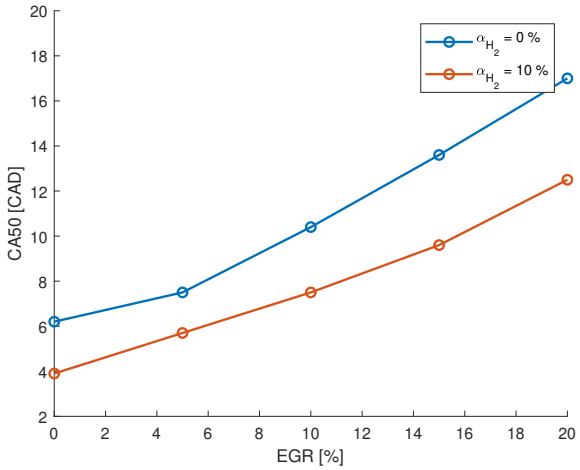

Figure 4.14: Comparison of CA50 with varying EGR percentage and H_2/methanol blend.

The CA50 is delayed with increasing EGR fraction. This is due to the longer ignition

delay and the longer combustion duration. In the case of the blended mixture, CA50 is always in advance compared to pure methanol. From 0 to 20 % EGR fraction, CA50 is delayed of 11 CAD for pure methanol while it is delayed of 7.8 CAD. This is due to a shorter combustion time and an advanced ignition delay than in the pure methanol case, as explained above. It can be seen that for the blended mixture with an EGR fraction of 10%, the CA50 is about 8 CAD. This value is the one for which the BMEP is optimized, which explains the peak of the IMEP for this operating condition. This indicates that the H_2/methanol blend fueled engine, for a given EGR fraction, must adopt an advanced ignition timing compared to pure methanol case to achieve improved engine efficiency.

Figure 4.15 shows the calculated in-cylinder temperature profile for the different percentages of EGR and H_2 addition. It can be seen that the maximum in-cylinder temperature is reduced with increasing EGR fraction.

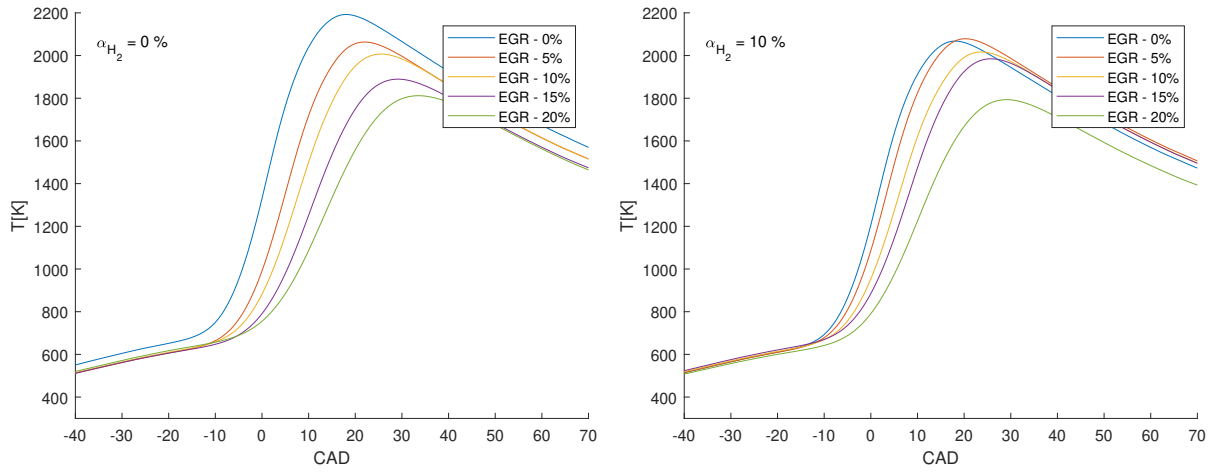

Figure 4.15: Comparison of the combustion duration with varying EGR percentage and H_2/methanol blend.

The reason is that the more inert gases in the cylinder, the more combustion heat is absorbed, which slows combustion and leads to a lower in-cylinder combustion temperature. Since H_2 has a higher adiabatic flame speed and adding H_2 results in a shorter combustion time, the peak is higher under blended conditions than pure methanol. However, this temperature difference is relatively small, which can be explained by the meager fraction of heat input that H_2 represents. Indeed, a 10% molar fraction of H_2 represents 5% of the total energy input. Since the H_2 helps the formation of the flame kernel, most of the H_2 is likely burned in the early combustion stage. If the energy input fraction of H_2 is increased, it is more likely to have a significant peak temperature difference than pure methanol with EGR. Moreover, trends in temperature indicate that a higher EGR fraction should accompany H_2/methanol blend to control the maximum cylinder temperature.

A parallel can be drawn between peak cylinder temperature and NOx formation: If the peak temperature decreases, NOx emissions will probably decrease. However, NOx in

H_2/methanol blend is likely to increase for a given EGR fraction compared to the pure methanol case, and the amplitude will depend on the H_2 blended fraction. As EGR increases, the in-cylinder temperature with H_2 addition will eventually decrease significantly, highlighting the importance of EGR on NOx emission control. Therefore, it is possible to decrease the in-cylinder temperature of the engine with EGR when running with a H_2/methanol blend, and thus decreasing NOx emissions.

4.2.2 Cyclic variability

Figure 4.16 shows the COV_{IMEP} variations with varying EGR for pure methanol and H_2/methanol blends. Figure 4.16 indicates that the COV_{IMEP} of the pure methanol case increases sharply with increasing EGR.

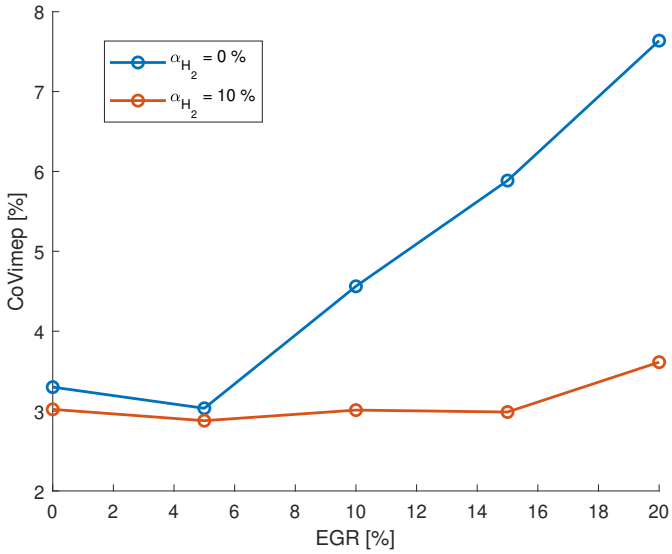

Figure 4.16: COV_{IMEP} with varying EGR percentage and H_2 substitution.

As the trend shows, the threshold value of 10% is most likely reached shortly after the EGR fraction of 20%. In comparison, the COV_{IMEP} of the H_2/methanol blend increases only slightly with increasing EGR. The cyclic variation of the engine is related to the combustion start, burn duration, and a longer burn duration usually leads to an increase in the cyclic variation of the engine. This is the observed phenomenon. The reason is that the longer burn time means more fuel is burned during the expansion stroke where the effect of turbulence is more pronounced than during the intake phase. Therefore, since the combustion time is shortened and the flammability limit of the mixture is extended with H_2, the COV_{IMEP} of the H_2/methanol mixture is relatively low compared to the case of pure methanol, especially at higher EGR fractions.

The introduction of a H_2/methanol blends enables to shorten and advance the combustion, which ultimately results in a more stabilized combustion. The COV_{IMEP} is nearly

constant throughout the whole set EGR fraction. For an EGR fraction of 20%, a 44% decrease in COV_{IMEP} is achievable compared to pure methanol case.
From 0 to 20 %, the COV_{IMEP} is increased by 4.2 % and 0.5% for respectively pure methanol and H_2/methanol blend.

4.3 Results uncertainties

Uncertainties over the data acquisition probes can be a matter of importance, especially because of uncertainties accumulation when computing quantities involving multiple ways of data recovery or probes. Mean values over a 300 cycles can also induce imprecision.

Uncertainties can be categorized into two main classifications: Type A and Type B. As clearly explained by Waldmann et al. in their Assessment of sensor performance [59], Type A evaluations of uncertainties result on the statistical analysis of a series of measurements. It involves the repeatability of the experiments conducted. Type B uncertainties cover other sources of information such as instruments and sensors data sheets.

4.3.1 Intake species uncertainties

The intake species quantities must be evaluated in an uncertainty point of view. The mass flow controllers used for the different gases have all Type B errors of less than 1%. The uncertainties brought by the MFCs can therefore be assumed to be negligible.

Howevern careful considerations must be made about the injector.

- First, the injection depends on the pressurization of the fuel tank. The same injection duration for different levels of pressures produces different mass flow rates. Although great care is taken by the authors to set the same pressure (i.e., 6 bar) at the beginning of each experiment, fixing it with needle pressure gauges cannot ensure negligible differences between experiments.

- Second, the injector is controlled by the MoTeC M84 ECU. This device is connected to a power supply. It must be noted that the reading of the voltage received by the ECU fluctuates a lot. This might generate variations in the signal sent by the ECU to the injector, inducing differences in mass flow rates from cycle-to-cycle. In addition, the software includes a number of interlocking compensations that can lead to a certain loss of accuracy if not properly addressed.

- Third, the injector chosen for the experiments is compatible with methanol with condition that it undergoes gasoline rinsing after each use. Despite the fact this operation is conducted at the end of each day of operation, methanol is corrosive and

might cause wear over time. Moreover, the fuel tank is observed to release small particles when purging it. Even if the amount of such particles is not impressive, it can be assumed that they might induce short-time blockages ever so often.

Colette & Gatin [45] worked with WDI and conducted an uncertainty analysis on the water mass injected. A similar process can be applied to the methanol injector employed in this master thesis. A noticeable difference is the fact water was injected into an environment undergoing large differences of pressure throughout time (i.e. the cylinder) whereas the present methanol injector sees its output figuring in the intake manifold, where pressure is relatively stable. Also, the pressure of injection is always kept constant in the case of the latter injector.

The global 95% confidence interval is computed on the basis of Equation 4.1.

$$U_{global} = \sqrt{U_y^2 + (A_1 U_x)^2 + U_{est}^2} \tag{4.1}$$

with the following terms:

- U_y: the 95% uncertainty on the measured mass, i.e. 95% of the Least Count (LC) of the weighing scale divided by two
  Sartorius 2102-1S scale: resolution = 0.01 g
- A_1: the coefficient from the linear regression approximating the injected mass per cycle $[\tilde{y}] = A_1[x] + A_0$, $[x]$ the duration of injection in [ms]
- U_x: the 95% of half the LC of the opening command, which is done by the ECU
- U_{est}: the uncertainty on the linear regression

The injection reaching a plateau after 40% of the opening duration, the linear regression is conducted on these first points. It is then supposed that the mass flow rate of the injector is uniform over a 40% opening. The uncertainties on the injected mass obtained vary between 10 and 14%. This threshold is on the high side although it should be pointed that methanol use in injectors can enhance wear even if gasoline rinsing occurs periodically.

4.3.2 Uncertainty on the IMEP and the IE

The following analysis is based on the methodology proposed by Pochet in its thesis on electrofuels in HCCI engines [39, 60]. The methodology is not fully detailed in the following development. The reader can therefore refer to this document to complete his or her understanding.

The IMEP is computed only based on pressure and volume, which are discrete data. Their derivatives can then be expressed in terms of discrete change (Δ). The uncertainty of

the IMEP is computed through Equation 4.2 with M being equal to V_d, the displacement volume, and by taking the upper bound for the pressure uncertainty (refer to [60]).

$$u_{IMEP} = \sqrt{\sum_{\theta=-180}^{180} \left[\left(\frac{\Delta V_\theta}{M} u_{p_\theta} \right)^2 + \left(\frac{p_\theta}{M} u_{\Delta V_\theta} \right)^2 + \left(\frac{-p_\theta V_\theta}{M^2} u_M \right)^2 \right]} \tag{4.2}$$

The global $U_{95,IMEP}$ uncertainty is evaluated for a data set from a methanol stoichiometric run without EGR or H_2 blend and with a spark advance of 21 CAD. It yields a 95% uncertainty on the IMEP of 0.64%, remaining below 1%. This results, if expressed in pressure units, becomes IMEP $\pm$ U_{95} = 6.42 $\pm$ 0.041 bar.

The uncertainty on the IE is also assessed by taking Equation 4.2 with M being the quantity of fuel energy injected per cycle. For the same experiment, IE $\pm$ U_{95} = 31.67 $\pm$ 3.0% is obtained. This higher result is attributed to the larger uncertainty on the injection that is developed in Section 4.3.1.

Conclusion

The present work experimentally investigated a methanol-fueled SI engine with synthetic EGR and H_2 blend with a particular interest in combustion stability. A methanol-fueled SI engine was implemented for this purpose. Experiments highlighted the stabilizing effect of H_2 on combustion for different dilution levels.

The first chapter introduced how methanol can be an exciting alternative to conventional fossil fuels in the context of an energy transition to net zero carbon. Its properties and application in SI engines were detailed. Then, EGR, its advantages, and a practical way to implement it experimentally were presented.

The modifications brought to implement the methanol-fueled SI engine were presented in the second chapter, and a description of the test bench running on methanol was given. An overview of the experimental procedure was also presented.

The third chapter presented the raw pressure data processing methodology to obtain interpretable results. First, the means of calibration of the data were presented. They consisted of determining the TDC offset, the effective compression ratio, the pressure filtering, and the pressure calibration. A sensitivity analysis of these parameters was then performed to highlight their importance in the post-processing procedure. Finally, the approach for calculating the important parameters for the combustion analysis of spark ignition engines and the multiple iteration loops involved were explained.

The results of the experimental study were presented and analyzed in the fourth and final chapter. First, the MBT timing for pure methanol operation was found at 21 CAD bTDC for an IMEP of 6.42 bar and an IE of 34.7%. In terms of power density and efficiency, this result must be nuanced: the amount of methanol injected was limited, preventing proper filling of the engine from operating under stoichiometric conditions at atmospheric intake pressure, the valve timing was not optimized, the original engine geometry was designed for DICI operation, and injection in the engine could not be optimized.

The introduction of EGR increased the engine's combustion instability, which resulted in a reduction in IMEP and IE. However, the hydrogen mixture effectively countered this phenomenon, decreasing combustion time and ignition delay and increasing peak cylinder pressure and temperature. H_2 blend resulted in a 2% increase in IE over the pure methanol case and 4.1% in the case of the highest EGR fraction. The COV_{IMEP} in the methanol case increased rapidly to a value of 8% for the highest EGR, while it was

maintained below 4% with hydrogen blend for the range of conditions tested. Hydrogen in small quantities can stabilize combustion when EGR is applied. Also, the in-cylinder peak temperature decreased as EGR increased, even for the hydrogen blend.

Although the results demonstrated the interest in using hydrogen to reduce the instability in methanol combustion, it would be interesting to improve the knowledge of the bench to increase the power density of the engine, as well as decrease combustion instability under stoichiometric conditions.

Outlook for the future

The use of hydrogen blending to improve combustion stabilization on an SI engine fueled by synthetic EGR diluted methanol was evaluated in this master's thesis. Although the results are conclusive, the extent of the hydrogen blend should be further evaluated. Different amounts of hydrogen blend should be applied to the intake mixture to characterize further the effect of hydrogen addition on the combustion of EGR diluted methanol.

Problems with the injector limited the inlet pressure to 0.7 bar to maintain stoichiometric conditions. Determination of the cause of such a restriction of the maximum injector mass flow must be completed. Then, further research should be conducted on the test bench with a higher inlet pressure, i.e., atmospheric pressure.

Bench improvement that would provide greater reliability on the test bed would be the addition of a position sensor at the camshaft. This would allow fuel to be injected only once per cycle, as opposed to twice per complete cycle, as this work did. Finally, the PFI could be done earlier to the intake line to enhance the homogenization of the methanol-air mixture.

Bibliography

[1] Allen et al. An ipcc special report on the impacts of global warming of 1.5řc above pre-industrial levels and related global greenhouse gas emission pathways, in the context of strengthening the global response to the threat of climate change, sustainable development, and efforts to eradicate poverty. pages 49–92, October 2018.

[2] National Oceanic and Atmospheric Administration (NOAA). Trends in atmospheric carbon dioxide. `https://gml.noaa.gov/ccgg/trends/global.html`.

[3] European Commission. Accords de paris. `https://ec.europa.eu/clima/eu-action/international-action-climate-change/climate-negotiations/paris-agreement_fr`.

[4] European commission. European green deal. `https://ec.europa.eu/clima/eu-action/european-green-deal_fr`.

[5] European Environment Agency. Greenhouse gas emissions from transport in europe. `https://ec.europa.eu/clima/eu-action/international-action-climate-change/climate-negotiations/paris-agreement_fr`.

[6] Dylan Carter. Eu greenhouse gas emissions above pre-pandemic levels. *The Brussels Times*, 2022.

[7] R. J. Pearson, J. W. G. Turner, and A. J. Peck. Gasoline-ethanol-methanol tri-fuel vehicle development and its role in expediting sustainable organic fuels for transport. 2009. Paper No. C678/016/09; IMechE Low Carbon Vehicles.

[8] Shishir Bhardwaj and Hamid Mostofi. Technical and business aspects of battery electric trucksmdash;a systematic review. *Future Transportation*, 2(2):382–401, 2022.

[9] Sebastian Verhelst, James WG Turner, Louis Sileghem, and Jeroen Vancoillie. Methanol as a fuel for internal combustion engines. *Progress in Energy and Combustion Science*, 70:43–88, 2019.

[10] Pallavi Gautam, Neha, S.N. Upadhyay, and S.K. Dubey. Bio-methanol as a renewable fuel from waste biomass: Current trends and future perspective. *Fuel*, 273:117783, 2020.

[11] Goeppert A. en Prakash lah, G.A. Chemical recycling of carbon dioxide to methanol and dimethyl ether: From greenhouse gas to renewable, environmentally carbon

neutral fuels and synthetic hydrocarbons. *The Journal of Organic Chemistry*, 46(49):25294–25307, 2021.

[12] Patrizio Battaglia, Giulio Buffo, Domenico Ferrero, Massimo Santarelli, and Andrea Lanzini. Methanol synthesis through co2 capture and hydrogenation: Thermal integration, energy performance and techno-economic assessment. *Journal of CO2 Utilization*, 44:101407, 2021.

[13] P. Galindo Cifre and O. Badr. Renewable hydrogen utilisation for the production of methanol. *Energy Conversion and Management*, 48(2):519–527, 2007.

[14] Zhi Tian, Yang Wang, Xudong Zhen, and Zengbin Liu. The effect of methanol production and application in internal combustion engines on emissions in the context of carbon neutrality: A review. *Fuel*, 320:123902, July 2022.

[15] Matt Brusstar and Marco Bakenhus. Economical, high-efficiency engine technologies for alcohol fuels. 01 2005.

[16] R.J. Nichols. The methanol story: A sustainable fuel for the future. *Journal of Scientific and Industrial Research*, 62:97–105, 01 2003.

[17] Utsumi S. Ota A. Kawatake K. et al. Nakata, K. The effect of ethanol fuel on a spark ignition engine. *SAE Technical Paper*, 2006.

[18] G R Neame, D P Gardiner, R W Mallory, V K Rao, M F Bardon, and V Battista. Improving the fuel economy of stoichiometrically fueled s.i. engines by means of egr and enhanced ignition – a comparison of gasoline, methanol and natural gas. 12 1995.

[19] G. M. Pannone and R. T. Johnson. Methanol as a fuel for a lean turbocharged spark ignition engine. *SAE Transactions*, 98:243–253, 1989.

[20] Matthew Brusstar, Mark Stuhldreher, David Swain, and William Pidgeon. High efficiency and low emissions from a port-injected engine with neat alcohol fuels. *SAE Transactions*, 111:1445–1451, 2002.

[21] A Koenig, W Lee, and W Bernhardt. Technical and economical aspects of methanol as an automotive fuel. 1 1976.

[22] Matthew J. Brusstar and Charles L. Gray. High efficiency with future alcohol fuels in a stoichiometric medium duty spark ignition engine. *SAE Transactions*, 116:1183–1190, 2007.

[23] Shenghua Liu, Eddy R. Cuty Clemente, Tiegang Hu, and Yanjv Wei. Study of spark ignition engine fueled with methanol/gasoline fuel blends. *Applied Thermal Engineering*, 27(11-12):1904–1910, 2007.

[24] David W. Naegeli, Paul I. Lacey, Matthew J. Alger, and Dennis L. Endicott. Surface corrosion in ethanol fuel pumps. *SAE Transactions*, 106:564–571, 1997.

[25] Vikram Kumar and Avinash Kumar Agarwal. Material compatibility aspects and development of methanol-fueled engines. pages 37–51, oct 2019.

[26] Tijl Jooris and Ward Suijs. *Improving part-load performance of a methanol-fuelled engine by means of exhaust gas recirculation*. PhD thesis, 2019.

[27] Héctor Climent, Vicente Dolz, Benjamín Pla, and David González-Domínguez. Analysis on the potential of egr strategy to reduce fuel consumption in hybrid powertrains based on advanced gasoline engines under simulated driving cycle conditions. *Energy Conversion and Management*, 266:115830, 2022.

[28] Shawn Rood, Salvador Eslava, Alexis Manigrasso, and Chris Bannister. Recent advances in gasoline three-way catalyst formulation: A review. *Proceedings of the Institution of Mechanical Engineers, Part D: Journal of Automobile Engineering*, 234(4):936–949, 2020.

[29] Haiqiao Wei, Tianyu Zhu, Gequn Shu, Linlin Tan, and Yuesen Wang. Gasoline engine exhaust gas recirculation a review. *Applied Energy*, 99:534–544, 2012.

[30] Khalid Al-Qurashi, Angela D. Lueking, and André L. Boehman. The deconvolution of the thermal, dilution, and chemical effects of exhaust gas recirculation (egr) on the reactivity of engine and flame soot. *Combustion and Flame*, 158(9):1696–1704, 2011.

[31] Bai-gang Sun, Dong-sheng Zhang, and Fu-shui Liu. Cycle variations in a hydrogen internal combustion engine. *International Journal of Hydrogen Energy*, 38(9):3778–3783, March 2013.

[32] Bin Huang, Erjiang Hu, Zuohua Huang, Jianjun Zheng, Bing Liu, and Deming Jiang. Cycle-by-cycle variations in a spark ignition engine fueled with natural gashydrogen blends combined with egr. *International Journal of Hydrogen Energy*, 34(19):8405–8414, 2009.

[33] Changming Gong, Xiankai Si, and Fenghua Liu. Comparative analysis on combustion and emissions between co2 and egr dilution gdi engine at half-load, stoichiometric and lean-burn conditions. *Fuel*, 309:122216, 2022.

[34] Subir Bhaduri, Hervé Jeanmart, and Francesco Contino. EGR control on operation of a tar tolerant HCCI engine with simulated syngas from biomass. *Applied Energy*, 227:159–167, October 2018.

[35] Ming Zheng, Graham T. Reader, and J. Gary Hawley. Diesel engine exhaust gas recirculationa review on advanced and novel concepts. *Energy Conversion and Management*, 45(6):883–900, April 2004.

[36] Zhi Tian, Yang Wang, Xudong Zhen, and Daming Liu. Numerical comparative analysis on performance and emission characteristics of methanol/hydrogen, ethanol/hydrogen and butanol/hydrogen blends fuels under lean burn conditions in SI engine. *Fuel*, 313:123012, April 2022.

[37] Shuofeng Wang, Changwei Ji, Bo Zhang, Xiaoyu Cong, and Xiaolong Liu. Effect of CO2 dilution on combustion and emissions characteristics of the hydrogen-enriched gasoline engine. *Energy*, 96:118–126, February 2016.

[38] Cheolwoong Park, Sangyeon Won, Changgi Kim, and Young Choi. Effect of mixing CO2 with natural gashydrogen blends on combustion in heavy-duty spark ignition engine. *Fuel*, 102:299–304, December 2012.

[39] Maxime Pochet. *Use of electrofuel blends in homogeneous-charge compression-ignition engines*. PhD Thesis, Ph. D. dissertation, UCL-Université Catholique de Louvain, 2020.

[40] Selim Tangöz, Selahaddin Orhan Akansu, Nafiz Kahraman, and Yusuf Malkoç. Effects of compression ratio on performance and emissions of a modified diesel engine fueled by HCNG. *International Journal of Hydrogen Energy*, 40(44):15374–15380, November 2015.

[41] Dinçer Akal, Semiha Öztuna, and Mustafa Kemalettin Büyükakn. A review of hydrogen usage in internal combustion engines (gasoline-Lpg-diesel) from combustion performance aspect. *International Journal of Hydrogen Energy*, 45(60):35257–35268, December 2020.

[42] Jianbing Gao, Xiaochen Wang, Panpan Song, Guohong Tian, and Chaochen Ma. Review of the backfire occurrences and control strategies for port hydrogen injection internal combustion engines. *Fuel*, 307:121553, January 2022.

[43] Jongtai Lee, Kwangju Lee, Jonggoo Lee, and Byunghoh Anh. High power performance with zero NOx emission in a hydrogen-fueled spark ignition engine by valve timing and lean boosting. *Fuel*, 128:381–389, July 2014.

[44] Kwang-Ju Lee, Thanh Cong Huynh, and Jong-Tai Lee. A study on realization of high performance without backfire in a hydrogen-fueled engine with external mixture. *International Journal of Hydrogen Energy*, 35(23):13078–13087, December 2010.

[45] Thomas Collette and Anthony Gatin. *Increasing HCCI power density through thermal stratification : impact of water direct injection*. PhD thesis, 2019.

[46] Ouz Ba, Mustafa Atakan Akar, Hasan Serin, Mustafa Özcanl, and Erdi Tosun. Variation of spark plug type and spark gap with hydrogen and methanol added gasoline fuel: Performance characteristics. *International Journal of Hydrogen Energy*, 45(50):26513–26521, 2020. The recent studies towards hydrogen production and fuel cells.

[47] Subir Swaraj Bhaduri. *Experimental studies on HCCI combustion of biomass syngas towards tar tolerant operation*. PhD thesis, UCL - Université Catholique de Louvain, 2015.

[48] Bosch Motorsport. *Lambda sensors*, April 2011.

[49] Yousef Najjar, Abad Almardini, and Amro Sawan. Comparison of performance using wide-band versus narrow-band oxygen sensors in gasoline engines. *Case Studies in Thermal Engineering*, 16:100552, October 2019.

[50] Autodata Training. Wide Band Oxygen Sensors, January 2015.

[51] Bosch LSU 4.9 is superior to LSU 4.2 sensors | News | ECOTRON.

[52] Emiliano Pipitone, Alberto Beccari, and Stefano Beccari. The experimental validation of a new thermodynamic method for tdc determination. 2007.

[53] F. Payri, P. Olmeda, C. Guardiola, and J. Martín. Adaptive determination of cut-off frequencies for filtering the in-cylinder pressure in diesel engines combustion analysis. *Applied Thermal Engineering*, 31(14):2869–2876, 2011.

[54] Estimation of the in-cylinder air/fuel ratio of an internal combustion engine by the use of pressure sensors.

[55] Lars Eriksson and Andreas Thomasson. Cylinder state estimation from measured cylinder pressure traces - a survey**this project was financed by the vinnova industry excellence center link-sic. *IFAC-PapersOnLine*, 50(1):11029–11039, 2017. 20th IFAC World Congress.

[56] Bonnie J. Mcbride, Sanford Gordon, Martin A. Reno, Sanford Gordon, and Martin A. Reno. Coefficients for calculating thermodynamic and transport properties of individual species. January 1993. Number: NASA-TM-4513.

[57] Jeffery A Massey. Indication of cylinder pressure rise rate by means of vibration and acoustic emissions of an internal combustion engine. 2008.

[58] Diming Lou, Yedi Ren, Yunhua Zhang, and Xia Sun. Study on the effects of egr and spark timing on the combustion, performance, and emissions of a stoichiometric natural gas engine. *ACS Omega*, 5(41):26763–26775, 2020. PMID: 33111003.

[59] Christoph Waldmann, Mario Tamburri, Ralf Prien, and Peer Fietzek. Assessment of sensor performance. *Ocean Science (OS)*, 6, 02 2010.

[60] Maxime Pochet, Hervé Jeanmart, and Francesco Contino. Uncertainty quantification from raw measurements to post-processed data: A general methodology and its application to a homogeneous-charge compressionignition engine. *International Journal of Engine Research*, 21(9):1709–1737, November 2020. Publisher: SAGE Publications.

Appendix A

A.1 PID

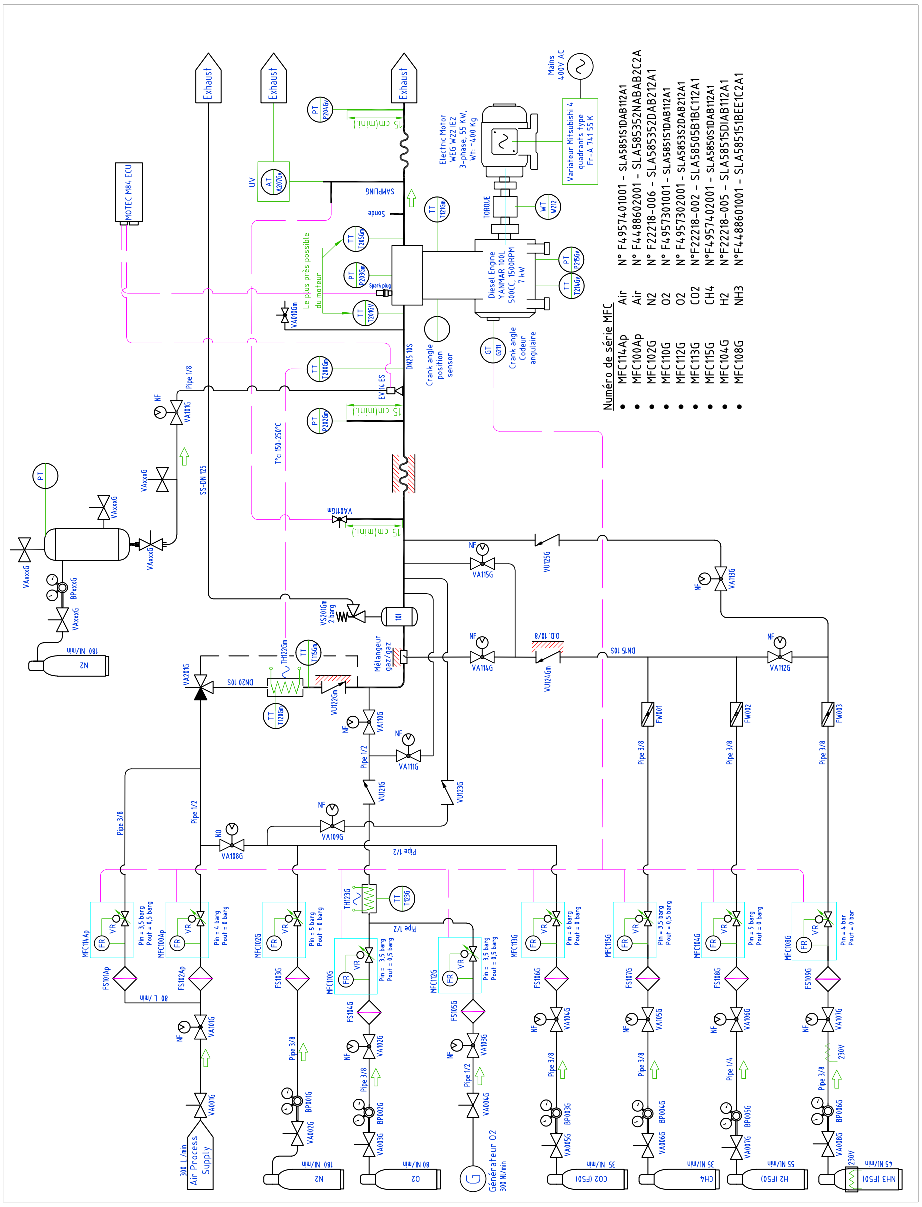

A.2 ATEX zoning

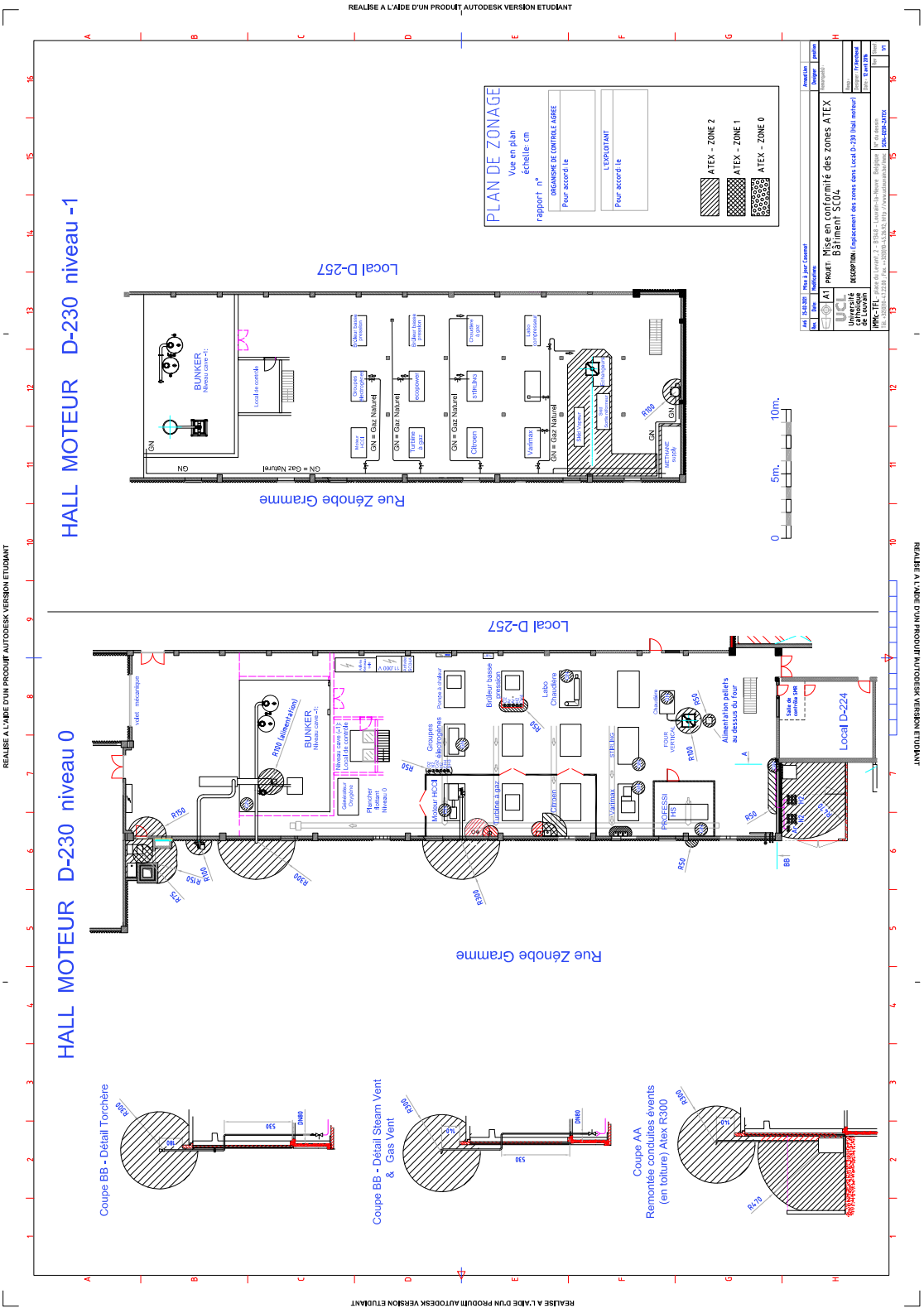

A.3 DRPE

1. Généralités

Dans le cadre des recherches menées sur les e-carburants, un moteur expérimental a été installé dans la plateforme CREDEM (casemate hall thermodynamique et procédés). Le moteur est originellement un moteur Diesel modifié pour fonctionner en mode Essence (allumage par étincelle). Celui-ci est interchangeable avec le moteur HCCI.
Le présent document est considéré comme un avenant du dernier DRPE en date.

2. Analyse de risque

2.1. Dispositif mis en place

L'utilisation du méthanol pour faire tourner le moteur essence nécessite la création d'une nouvelle conduite de carburant pour alimenter celui-ci. Le nouveau réservoir de carburant se compose d'un réservoir à 6 vannes, numérotées comme indiqué sur l'image suivante.

- La vanne **1** sert à verser le méthanol dans le réservoir. Elle sert aussi à verser de l'essence dans le réservoir pour rincer l'injecteur après usage.
- La vanne **2** est la vanne par laquelle l'azote est fourni à partir d'une bouteille placée à côté du réservoir, à l'endroit prévu à cet effet avec une chaine. Pour notre application, il ne nécessite d'utiliser une pression de 6 bar. La bouteille d'azote adjacente est munie d'un d'étendeur **7** ainsi que d'un clapet de sécurité **8**.
- La vanne **3** est la sortie du réservoir et assure le raccordement aux canalisations vers l'injecteur.
- La vanne **4** ne sert que lorsqu'il est nécessaire de purger le réservoir et la conduite de carburant.
- La vanne **5** est une vanne de sécurité reliée à la vanne VA101G visible sur le PID en annexe. Si une urgence survient et que cette dernière est fermée, cela permet de couper automatiquement la liaison entre le réservoir et les conduites en aval.
- Le numéro **6** désigne la soupape de sécurité qui s'ouvre dès que la pression dans le réservoir dépasse les 7.5 bar. De plus, un manomètre y a été apposé pour un meilleur contrôle de la pression.

2.2. Analyse du risque d'explosion

La mise en place de ce système induit des risques répertoriés dans cette section.

2.2.1. Flammabilité du méthanol et zone ATEX induite : Réservoir

Le point éclair du méthanol est de 12°C. Le méthanol pur (concentration de méthanol à 100 %) s'enflamme beaucoup moins rapidement dans les environnements ouverts et restreints que l'essence. La faible volatilité du méthanol produit plus ou moins un tiers du volume de vapeur par unité de temps provenant de la même source de volume que l'essence. De plus, puisque sa densité de vapeur est très proche de celle de l'air (rapport plus ou moins 1:1) et son coefficient de diffusion est 2,5 fois supérieure à celle de l'essence, la vapeur produite est beaucoup plus rapidement dispersée que la vapeur d'essence. De plus, la limite inférieure d'inflammabilité du méthanol est telle qu'une concentration molaire de 6 % (LIE) doit être atteinte pour que l'inflammation se produise, l'inflammabilité supérieure limité étant de 36 % (UEL). Ces concentrations présentent un risque d'inflammabilité pour des températures comprises entre 12 et 43 °C.

2.2.2. Flammabilité du méthanol et zone ATEX induite : Conduite

L'utilisation de conduite d'alimentation avec un nombre de raccords réduit au minimum permet d'éliminer des sources éventuelles d'émission. Les raccords subsistants sont des raccords à double férule permettent sécurité et une étanchéité suffisante pour écarter la prise en compte d'une éventuelle fuite le long de la conduite.

Le contrôle de l'étanchéité des conduites avant utilisation de l'installation permet de s'affranchir des potentielles fuites au niveau des raccords et flexibles.

Afin d'effectuer ce test, se référer au document « Procédure d'utilisation ». Il y a une section dédiée au test d'étanchéité pour faire présent à l'utilisateur du banc qu'au début de chaque campagne expérimentale il faut faire ce test.

Réservoir de stockage de carburant inflammable :

Source d'émission	Récipient fuite ou mal fermée (bouteille vide)
Faire disparaître	Non
Réduire	Oui par une procédure de stockage

Conduites et raccords :

Source d'émission	Discontinuité entre élément
Faire disparaître	Non
Réduire	Oui par une procédure de contrôle installation

Description des sources d'inflammation (selon norme EN 1127-1). L'entretient et le nettoyage ne peut se faire que quelques heures après utilisation lorsque le moteur est froid et lorsque l'alimentation du banc et l'alimentation électrique sont coupées.

Sources d'inflammation		Sources			
		F	E	N	D
F= Fonctionnement, E = Entretien, N = nettoyage, D = Dysfonctionnement					
Surfaces chaudes		**X**			
Flammes et gaz chauds		**X**			
Étincelles produites mécaniquement		**X**			
Installations électriques		**X**			**X**
Courants transitoires, protection cathodique contre la corrosion					

Électricité statique		X			X
Foudre					
Ondes électromagnétiques comprises dans une gamme de fréquences de 9 kHz à 300 GHz					
Ultrasons					
Compression adiabatique, ondes de choc, écoulement de gaz					
Réactions chimiques		X			

2.2.3. Explication de l'évaluation du risque

La méthodologie utilisée pour l'évaluation du risque est celle de Graham Kinney, suivant la norme EN 1050.

Graham Kinney :
La méthode est basée sur un calcul du risque en multipliant les facteurs suivants les uns avec les autres : la gravité de la blessure potentielle (G), la probabilité que la blessure se produise (P) et le facteur d'exposition au risque (E).

Les codes suivants sont appliqués pour les différents facteurs :

Gravité :	G	1	Blessure sans incapacité de travail
	G	3	Incapacité de travail
	G	7	Blessure irréversible, invalidité
	G	15	Un mort
	G	40	Plusieurs morts
	G	100	De nombreux morts
Probabilité :	P	0,2	Pratiquement impossible
	P	0,5	Concevable mais improbable
	P	1	Improbable mais possible dans les cas limites
	P	3	Inhabituel
	P	6	Peut se produire
	P	10	Pouvant être attendu
Exposition :	E	0,5	Très rarement (moins d'une fois par an)
	E	1	Rarement (tous les ans)
	E	2	Parfois (tous les mois)
	E	3	De temps en temps (toutes les semaines)
	E	6	Régulièrement (tous les jours)
	E	10	En permanence

Risque = G x P x E

Risque	
0 ... 20	**Risque acceptable**
20 ... 50	**Risque potentiel**
50 ... 200	**Risque important**
200 ... 400	**Risque élevé**
400 ...	**Risque très élevé**

2.2.4. Evaluation du risque

La production d'une atmosphère explosive dans le cadre de ce prototype est le fait d'un mélange dans des proportions adéquates de combustibles (à déterminer selon expérience) d'une part et d'oxygène ou d'air d'autre part.

Ce mélange pourrait se produire dans la casemate, si l'une des conduites venait à rompre. Il nous faut être certain de ne pas créer une ATEX dans ce cas de figure. Il a été calculé (voir Annexe) que la vitesse moyenne de l'air aux alentours de la ligne de méthanol devait être de 0.21 m/s.
Or la ventilation de la casemate en mode « automatique » permet d'obtenir une vitesse d'air autour du moteur de 2.9 m/s et en mode « manuel » (à puissance maximale) une vitesse de 5.84 m/s.

On peut donc conclure que si une ou plusieurs ruptures viennent à se produire, la ventilation de la casemate est suffisante pour éviter la formation d'une zone ATEX.
Il ne peut donc pas y avoir de formation d'un mélange explosif dans les conditions normales d'utilisation de l'installation.

Il n'y a donc que le réservoir de méthanol qui est dans des zones ATEX étant donné les modifications et les mesures mise en place décrites dans l'analyse de risque ci-dessous.

Installation		Moteur HCCI						
Quand		**Sources du danger**		**Risque**				
En fonctionnement	**X**	*Source d'émission*	Fuite aux raccords ou dans la conduite d'admission	Risque d' explosion et d' incendie	G	P	E	R
Maintenance		*Source d'ignition*	Électricité statique, dispositif électrique…		7	1	6	42
Nettoyage		*Ventilation*	Extracteur casemate		Risque non acceptable			
Dysfonctionnement								
Mesures				**Risque**				
Adaptation constructive				Risque d' explosion et d' incendie après la prise des mesures	G	P	E	R
Éviter les sources d'émissions		Vérification de l'étanchéité à chaque nouvelle campagne Férules double joints et/ou raccords soudés certifiés ATEX			7	0.2	6	8.4
Éviter les sources d'ignition		Suivre la procédure de démarrage : activer la ventilation de la casemate			Risque acceptable			
Formation		Formation sur les risques d'explosion Procédure de travail						
Signalisation		Placement des pictogrammes et marquage de la zone avec risque d'explosion						

Zone ATEX concernant le dispositif (Voir plan de zonage en Annexe) :

Bonbonnes de gaz : Zone 2 dans une sphère de 50 cm autour de la tête des bonbonnes.
Arrivée de gaz naturel : Zone 2 dans une sphère de 50 cm dans la cave sous le banc.
Sortie soupape de sureté : Zone 2 dans une sphère de 3 m autour de la sortie de la soupape de sureté à l'extérieur du bâtiment
Réservoir de méthanol : Zone 2 dans une sphère de 50cm autour de la tête du réservoir.
Zone 2 dans une sphère de 50 cm autour de la vanne de purge, sous le réservoir.
La zone de 1 m de diamètre étant majorée car le réservoir ne pourra contenir que 5l maximum de méthanol à la fois, le reste du réservoir étant pressurisé par un gaz inerte (azote) à une pression entre 3 et 7 bar.

3. Procédures de sécurité

Les procédures de remplissage et de purge ne sont pas reprises dans ce document pour éviter toute redondance avec le mémoire dans lequel cette analyse s'insère en annexe.

A.4 Filling procedure

The numbers in the following procedure refer to Figure 2.6.

1. Turn on basement extraction and bunker (casemate) ventilation.
2. Turn on electrical cabinet inside the bunker.
3. Wear gloves and security glasses.
4. Check that all the valves are on closed position. If a valve is open, close it.
5. Check that pressure in the fuel tank is at 0 barg on pressure gauge 6.
6. Open valve 1 to minimum if the tank is pressurized to allow it to depressurize.
7. Open fully valve 1.
8. Pour methanol in with the help of a funnel. Maximum 5 liters.
9. Close valve 1.
10. Open security valve 8 (red) of the nitrogen bottle.
11. Set pressure on the gauge 7 placed on the nitrogen bottle.
12. Open slowly valve 2 for pressurization of the fuel tank, until the valve is fully open. The gauge 6 should read the same as 7.
13. Launch LabVIEW control program and open valve VA101G. This will open security valve 5.
14. Check the line is closed (injector well fastened on the end).
15. Open slowly valve 3 until fully open.

A.5 Purging procedure

The numbers in the following procedure refer to Figure 2.6.

1. Check the basement extraction and bunker (casemate) ventilation are on.
2. Check the electrical cabinet inside the bunker is on.
3. Close valve 5 on the LabVIEW program (linked to valve VA101G).
4. Wear gloves and the gas mask reserved for this purpose.
5. Close security valve 8 and valve of the pressure gauge 7 on the nitrogen bottle.
6. Close valves 2 and 3 on the fuel tank.
7. Open valve 1 cautiously until depressurization the fuel tank.
8. Check that pressure in the fuel tank is at 0 barg on pressure gauge 6.
9. Place a funnel with the appropriate container under valve 4.
10. Open valve 3 fully.
11. Open slowly valve 4 until a moderate flow establishes at its output, while securing the funnel and avoid spillage.
12. Once the flow stops, close valve 4 and 3.

A.6 New shape piston bowl

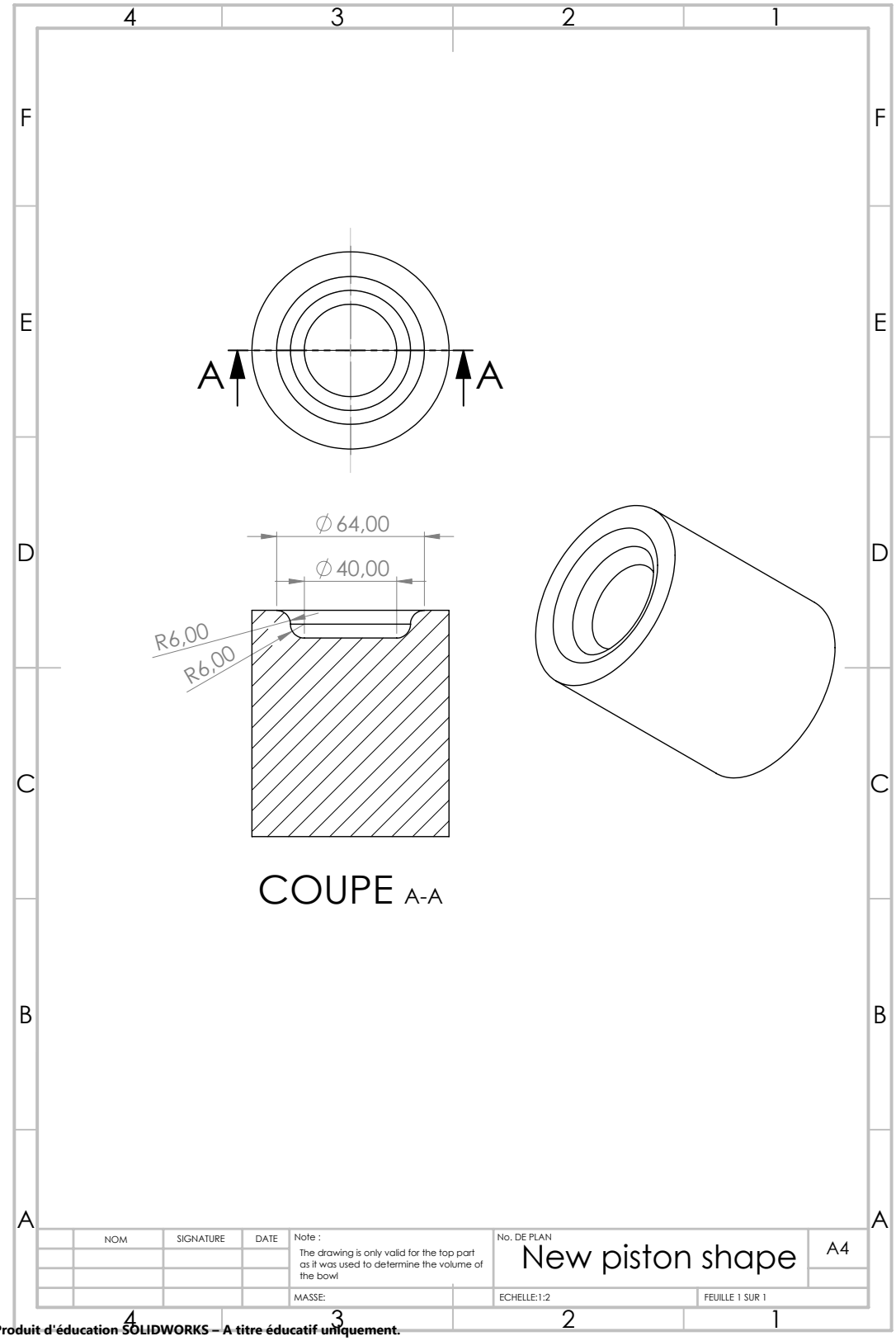

A.7 Specific heat coefficients

Species	T[K]	a_1	a_2	a_3	a_4	a_5
Nitrogen	T $\geq$ 1000	2.95257	$1.39690 \cdot 10^{-3}$	$-4.92631 \cdot 10^{-7}$	$7.86010 \cdot 10^{-11}$	$-4.60755 \cdot 10^{-15}$
N_2	T <1000	3.53100	$-1.23660 \cdot 10^{-4}$	$-5.02999 \cdot 10^{-7}$	$2.43530 \cdot 10^{-9}$	$-1.40881 \cdot 10^{-12}$
Oxygen	T $\geq$ 1000	3.66096	$6.56365 \cdot 10^{-4}$	$-1.41149485 \cdot 10^{-7}$	$2.05797 \cdot 10^{-11}$	$-1.29913 \cdot 10^{-15}$
O_2	T <1000	3.78245	$-2.99673 \cdot 10^{-3}$	$9.847 \cdot 10^{-6}$	$-9.68129 \cdot 10^{-9}$	$3.243728 \cdot 10^{-12}$
Methanol	T $\geq$ 1000	3.60134	$1.02430 \cdot 10^{-2}$	$-3.59985 \cdot 10^{-6}$	$5.72505 \cdot 10^{-10}$	$-3.3911 \cdot 10^{-14}$
CH_3OH	T <1000	5.71539	$-1.52309 \cdot 10^{-2}$	$6.52441 \cdot 10^{-5}$	$-7.10806 \cdot 10^{-8}$	$2.61352 \cdot 10^{-11}$
Hydrogen	T $\geq$ 1000	2.9328	$8.26607 \cdot 10^{-4}$	$-1.46402 \cdot 10^{-7}$	$1.54100 \cdot 10^{-11}$	$-6.88804 \cdot 10^{-16}$
H_2	T <1000	2.34433	$7.98052 \cdot 10^{-3}$	$-1.94781 \cdot 10^{-5}$	$2.01572 \cdot 10^{-8}$	$-7.37611 \cdot 10^{-12}$
Carbon dioxide	T $\geq$ 1000	4.63659	$2.74131 \cdot 10^{-3}$	$-9.95828 \cdot 10^{-7}$	$1.60373 \cdot 10^{-10}$	-9.16103^{-15}
CO_2	T <1000	2.35677	$8.98459 \cdot 10^{-3}$	$-7.12356 \cdot 10^{-6}$	$2.45919 \cdot 10^{-9}$	$-1.43699 \cdot 10^{-13}$
Water	T $\geq$ 1000	2.67703	$2.97318 \cdot 10^{-3}$	$-7.73769 \cdot 10^{-7}$	$9.44336 \cdot 10^{-11}$	$-4.26900 \cdot 10^{-15}$
H_2O	T <1000	4.19864	$-2.03643 \cdot 10^{-3}$	$6.52040 \cdot 10^{-6}$	$-5.48797 \cdot 10^{-9}$	$1.77197 \cdot 10^{-12}$

Table A.1: Coefficients for constant pressure specific heat.

UNIVERSITÉ CATHOLIQUE DE LOUVAIN
École polytechnique de Louvain
Rue Archimède, 1 bte L6.11.01, 1348 Louvain-la-Neuve, Belgique | **www.uclouvain.be/epl**